Active galactic nuclei emission line diagnostics and the mass-metallicity relation up to redshift z ∼ 2: the impact of selection effects and evolution

Stéphanie Juneau, Frederic Bournaud, Stéphane Charlot, Emanuele Daddi, David Elbaz, Jonathan Trump, Jarle Brinchmann, Mark Dickinson, Pierre-Alain Duc, Raphaël Gobat, et al.

ApJ; Accepted for publication
Preprint typeset using LaTeX style emulateapj v. 5/2/11

AGN EMISSION LINE DIAGNOSTICS AND THE MASS-METALLICITY RELATION UP TO REDSHIFT $z \sim 2$: THE IMPACT OF SELECTION EFFECTS AND EVOLUTION

Stéphanie Juneau[1,2], Frédéric Bournaud[1], Stéphane Charlot[3], Emanuele Daddi[1], David Elbaz[1], Jonathan R. Trump[4,5], Jarle Brinchmann[6], Mark Dickinson[7], Pierre-Alain Duc[1], Raphael Gobat[1], Ingrid Jean-Baptiste[1,8], Éméric Le Floc'h[1], M. D. Lehnert[8,3], Camilla Pacifici[9,3], Maurilio Pannella[1], and Corentin Schreiber[1]

ApJ; Accepted for publication

ABSTRACT

Emission line diagnostic diagrams probing the ionization sources in galaxies, such as the Baldwin-Phillips-Terlevich (BPT) diagram, have been used extensively to distinguish AGN from purely star-forming galaxies. Yet, they remain poorly understood at higher redshifts. We shed light on this issue with an empirical approach based on a $z \sim 0$ reference sample built from ∼300,000 SDSS galaxies, from which we mimic selection effects due to typical emission line detection limits at higher redshift. We combine this low-redshift reference sample with a simple prescription for luminosity evolution of the global galaxy population to predict the loci of high-redshift galaxies on the BPT and Mass-Excitation (MEx) diagnostic diagrams. The predicted bivariate distributions agree remarkably well with direct observations of galaxies out to $z \sim 1.5$, including the observed stellar mass-metallicity (MZ) relation evolution. As a result, we infer that high-redshift star-forming galaxies are consistent with having *normal* ISM properties out to $z \sim 1.5$, after accounting for selection effects and line luminosity evolution. Namely, their optical line ratios and gas-phase metallicities are comparable to that of low-redshift galaxies with equivalent emission-line luminosities. In contrast, AGN narrow-line regions may show a shift toward lower metallicities at higher redshift. While a physical evolution of the ISM conditions is not ruled out for purely star-forming galaxies, and may be more important starting at $z \gtrsim 2$, we find that reliably quantifying this evolution is hindered by selections effects. The recipes provided here may serve as a basis for future studies toward this goal. Code to predict the loci of galaxies on the BPT and MEx diagnostic diagrams, and the MZ relation as a function of emission line luminosity limits, is made publicly available.

Subject headings: galaxies: active — galaxies: evolution — galaxies: fundamental parameters — galaxies: Seyfert — galaxies: star formation

1. INTRODUCTION

Nebular emission lines can reveal crucial information on the ionized gas content in galaxies. In particular, several optical emission line diagnostics have been developed to probe gas properties such as metallicity, ionization parameter, electron density and temperature (Osterbrock & Ferland 2006), which can in turn provide additional insights on the source of ionization of the gas. An important application is thus the identification of active galactic nuclei (AGNs), which leave strong signatures on nebular line ratios such as [O III] λ5007/Hβ and/or [N II] λ6584/Hα. These two line ratios form the most traditional version of the BPT diagram (Baldwin et al. 1981; Veilleux & Osterbrock 1987). The latter has been calibrated with both a theoretical approach (Kewley et al. 2001; Stasińska et al. 2006; Kewley et al. 2013a) and empirically with low-redshift galaxies (Kauffmann et al. 2003).

There are now questions about the applicability of low-redshift nebular line diagnostics to higher-redshift objects. A number of studies suggest that high-redshift galaxies are offset from the locus of low-redshift reference samples on the standard BPT diagram ([O III] λ5007/Hβ vs. [N II] λ6584/Hα) (e.g., Shapley et al. 2005; Erb et al. 2006; Trump et al. 2013; Newman et al. 2014; Holden et al. 2014). While there are a few hypotheses, the cause of this offset is not yet fully explained. For example, it was suggested that high-redshift galaxies may have had different H II region conditions (such as electron densities, temperatures, pressures, etc.) relative to the bulk of star-forming galaxies (Brinchmann et al. 2008; Liu et al. 2008; Hainline et al. 2009; Lehnert et al. 2009; Rigby et al. 2011; Ly et al. 2014). It was suggested (Lehnert et al. 2013; Shirazi et al. 2013) that this may be due to galaxies globally forming their stars with a higher surface density in the past, which has been inferred from infrared luminosity surface densities (Reddy et al. 2012) and galaxy infrared SED fitting (Magdis et al. 2012).

However, other studies claim that the offsets on excitation diagrams are instead caused by an increased contribution from AGN (Groves et al. 2006; Wright et al.

[1] CEA-Saclay, DSM/IRFU/SAp, 91191 Gif-sur-Yvette, France
[2] stephanie.juneau@cea.fr
[3] UPMC-CNRS, UMR 7095, Institut d'Astrophysique de Paris, 75014, Paris, France
[4] University of California Observatories/Lick Observatory, University of California, Santa Cruz, CA 95064, USA
[5] Hubble Fellow; Department of Astronomy and Astrophysics, 525 Davey Lab, The Pennsylvania State University, University Park, PA 16802, USA
[6] Leiden Observatory, Leiden University, P.O. Box 9513, 2300 RA Leiden, The Netherlands
[7] National Optical Astronomy Observatory, 950 North Cherry Avenue, Tucson, AZ 85719, USA
[8] GEPI, Observatoire de Paris, UMR 8111, CNRS, Université Paris Diderot, 5 place Jules Janssen, 92190, Meudon, France
[9] Yonsei University Observatory, Yonsei University, Seoul 120-749, Republic of Korea

2010; Trump et al. 2011), which would shift the galaxies in a similar way (Kewley et al. 2013a). If there were a higher incidence of AGN in galaxies in the past we may expect a steeper ionization profile and thus varying emission line strengths. It is crucial to disentangle the source of ionization in galaxies (young stars vs. AGN) in order to interpret and derive important quantities in galaxy evolution studies like star formation rates (SFRs), metallicities, and gas dynamics, but also to understand the interplay between black hole growth and stellar growth in galaxies.

Furthermore, another complication arises because intermediate- and high-redshift galaxy samples used thus far may suffer from strong selection biases due to the emission line detection limits. Relative to existing large spectroscopic sample at low redshifts (e.g., SDSS), only galaxies with intrinsically luminous lines can be detected at intermediate to high redshifts. These potential selection biases have been mostly neglected thus far, and will be explored in this Paper along with genuine evolutionary trends. As we will show, emission line detection limits add complexity to the problem, but not taking them into account can yield misguided interpretations of how galaxy properties evolve with redshift.

In addition to the traditional BPT-[N II] diagnostic diagram, we revisit an alternative diagram using stellar mass in place of [N II]/Hα (the Mass-Excitation (MEx) diagnostic diagram from Juneau et al. 2011, hereafter J11). The MEx diagram has the advantage of requiring only the [O III]/Hβ emission lines, which are more widely separated in wavelength and therefore easier to resolve spectroscopically than Hα and [N II]. Furthermore, they be can observed to higher redshift in any given wavelength regime. In optical spectra, [N II]/Hα are available out to $z \sim 0.45$ whereas [O III]/Hβ can be observed out to $z \sim 0.9$. Similarly, NIR spectra in the K band cover [N II]/Hα out to $z \sim 2.5$ but [O III]/Hβ out to $z \sim 3.7$. Another advantage of the MEx diagram is its probabilistic approach. For a given location on the MEx plane, and given the measurement errors, the MEx diagram yields the probability that the galaxy hosts an AGN. This method has a built-in uncertainty in the sense that ambiguous cases will have a low or intermediate AGN probability, and is well suited for statistical studies because the AGN probabilities can be used as statistical weigths to weigh for (or against) AGN. On the other hand, one might expect the MEx diagram to be more sensitive to evolution of the stellar-mass metallicity (MZ) relation (Savaglio et al. 2005; Shapley et al. 2005; Erb et al. 2006; Yabe et al. 2012; Zahid et al. 2013a), than the traditional BPT. We will show that an improved treatment of emission-line detection limit mitigates such bias by directly accounting for appropriate gas-phase metallicities when building a tailored low-redshift comparison sample for each survey.

The aim of this Paper is twofold. First, we provide improved AGN diagnostics that account for redshift-dependent effects. More specifically, we revisit both the original BPT diagram and more recent MEx diagram in order to disentangle selection and evolution effects, and to improve their applicability to a broad range of redshifts. In addition, this work reveals insight into the ISM conditions in higher redshift galaxies, once the selection effects are taken into account.

The Paper is organized as follows. We describe the galaxy samples used for low-redshift calibration and higher redshift applications in Section 2, followed by the low-redshift revision of the MEx demarcations in Section 3. The results (Section 4) include empirical predictions of the redshift evolution of the BPT and MEx diagrams including both genuine evolution and selection effects due to line detection limits (Section 4.1). These predictions are confronted with observations out to $z \sim 2$ (Section 4.2), and compared to theoretical predictions from Kewley et al. (2013a) in Section 4.3. The implications for the high-redshift application of emission line diagnostic diagrams are discussed in Section 5, including the stellar mass-metallicity relation, before the main findings are summarized in Section 6. Throughout this paper, we assume a flat ΛCDM cosmology ($\Omega_m = 0.3$, $\Omega_\Lambda = 0.7$, and $h = 0.7$) and a Chabrier (2003) initial mass function (IMF).

2. SAMPLE SELECTION

2.1. *Low-redshift galaxy sample*

The low-redshift emission-line galaxy sample is built from the Sloan Digital Sky Survey (SDSS) DR7 (Abazajian et al. 2009). The first selection criteria ensure that the galaxies are primary targets ($SCIENCEPRIMARY = 1$), and have a redshift determination in the range of interest ($0.04 < z < 0.2$). The lower and higher redshift cuts are imposed in order to, respectively, avoid strong aperture effects ($z > 0.04$) and offer a good compromise between detecting galaxies with intrinsically weak lines and obtaining better statistics on Seyferts ($z < 0.2$), following a similar approach to that of Kewley et al. (2006); Yuan et al. (2010).

From a primary sample of 426,367 galaxies, we further select 299,098 galaxies for which the [O III] λ5007/Hβ and [N II] λ6584/Hα line ratios are detected. Removing 5,469 galaxies with a missing or invalid stellar mass ($< 10^6\ M_\odot$), we obtain a sample of 293,629 galaxies with a median redshift of $z = 0.09$. We call this emission-line galaxy sample the $z \sim 0$ *SDSS prior sample* because it will be used as a set of priors to calculate the probability of galaxies hosting AGN given certain observables (namely stellar mass and [O III]/Hβ ratio) following the MEx method developed by J11.

Emission line fluxes were obtained from the Value Added Catalogs developed by the Max-Planck Institute for Astronomy (Garching) and John Hopkins University (MPA/JHU)[10], following the methodology described by Tremonti et al. (2004). We apply two corrections to the measurements listed in the Value Added Catalogs. First, we apply a correction to Hβ fluxes which were found to be underestimated by ΔEW = 0.35Å(Groves et al. 2012) because of the change in stellar population models between DR4 and DR7 (Charlot & Bruzual 2007 (CB07), instead of Bruzual & Charlot 2003, (BC03)). The corrected Hβ line fluxes are thus consistent with the use of the BC03 models for fitting the stellar continuum (and stellar absorption), like was done with SDSS DR4 spectra. Second, we augment the catalog's formal line flux uncertainties to represent more closely the true uncertainties by comparing emission line measurements

[10] http://www.mpa-garching.mpg.de/SDSS/DR7/

made on duplicate observations of the same galaxies (Appendix A).

Traditionally, emission-line galaxies are selected to have detections with a given signal-to-noise ratio (S/N), such as S/N> 3, for all four BPT-[N II] lines ([O III] λ5007, Hβ, [N II] λ6584, Hα). To obtain a more complete sample, and because the BPT diagram deals with line ratios, the detection limit is applied to the emission line ratios rather than to the individual lines. We require that the emission line *ratios* have S/N> 2.12 ($= 3/\sqrt{2}$), where the lower limit is equivalent to each line being detected at exactly 3σ. This cut furthermore includes combinations of a poorly-detected line ($< 3\sigma$) with a strongly-detected line provided the overall ratio is constrained to better than S/N=2.12. This modified approach yields a $\sim 20\%$ larger and therefore more complete census of emission-line galaxies, spanning a wider range of intrinsic properties. Relative to the more traditional approach, we include more numerous massive, metal-rich star-forming galaxies, as well as LINERs and *retired* galaxies, all of which tend to have comparatively faint [O III] λ5007 lines (Cid Fernandes et al. 2010, 2011).

This $z \sim 0$ SDSS prior sample is used to perform a new base calibration of the MEx diagnostic diagram at low redshift. However, when comparing to higher redshift samples, we revert to the typical method of imposing an individual line S/N> 3 cut for [O III] and Hα. This choice does not have a noticeable impact on the results presented in this paper, which concerns galaxies with fairly luminous lines that tend to be individually detected above 3σ. For example, at $\log(L_{\mathrm{H}\alpha,[\mathrm{O\ III}]}[\mathrm{erg\,s^{-1}}])> 39.9$, the lowest luminosity cut employed in this paper, only 0.8% of emission-line galaxies fail the S/N>3 criterion for either Hα or [O III].

Lastly, the emission-line sample is classified for the presence of AGN using the BPT-[N II] diagnostic diagram (Baldwin et al. 1981). Galaxies below and to the left of the Kauffmann et al. (2003) demarcation are considered star-forming, while the galaxies above and to the right of the Kewley et al. (2001) demarcation are AGN, and the galaxies between the lines are often called composites. Galaxies from the Kewley et al. (2001) AGN region can be further classified into Seyfert 2 (Sy2) or LINER based on their location on the BPT-[S II] diagram (Veilleux & Osterbrock 1987) using, for example, the division developed by Kewley et al. (2006)[11]. In this work, however, the LINER population is naturally removed by the emission line limits, effectively excluding the weak emission lines of LINER galaxies. Thus, most of our analyses apply to the star-forming, composite, and Sy2 classes.

We choose to treat composite and Sy2 galaxies as both hosting AGN. As argued by Salim et al. (2007), galaxies in the composite region have higher SFRs compared to those in the AGN region, such that the bulk of the difference from AGN to composite may simply be a weaker contrast between star formation and AGN lines. There is also good X-ray evidence (for both individual sources and stacked data) that most composite galaxies genuinely host AGNs (e.g., Juneau et al. 2011; Trouille et al. 2011; Trump et al. 2011). A few authors argue that some composite galaxies have line ratios influenced by shock activity rather than AGN (Rich et al. 2011; Newman et al. 2014), but these tend to be rare starbursts and not galaxies representative of the bulk population at $z \sim 0$ or $z \sim 2$. Instead, most composite galaxies are likely to correspond to a transition phase between starburst- and AGN-dominated systems (Yuan et al. 2010), in agreement with the concept of varying contrast between AGN and star formation emission and our categorization of composite galaxies as AGN.

2.2. *High-redshift galaxy samples*

The intermediate to high redshift galaxies used in this work were selected from the following:

- $0.3 < z < 1$ galaxies with $R_{AB} < 24.3$ and < 24.1 from the TKRS and DEEP2 redshift surveys, respectively (J11);
- $z \sim 1.4$ galaxies with $K < 23.9$, $1.2 < z_{phot} < 1.6$, $M_\star > 10^{9.5}\ M_\odot$ from the SXDS/UDS[12] fields with NIR spectra (Yabe et al. 2012, hereafter Y12);
- $z \sim 1.5$ emission-line selected galaxies from the GOODS-S field with NIR spectra (Trump et al. 2013, hereafter T13);
- $z \sim 2$ galaxies from the SINS/zC-SINF survey, GOODS-N and Q2343 fields, with NIR spectra, and selected by Newman et al. (2014, hereafter N14).

At $0.3 < z < 1$, optical spectroscopy was obtained from the Team Keck Redshift Survey[13] (TKRS Wirth et al. 2004) in GOODS-N, and from the DEEP2 Galaxy Redshift Survey (hereafter DEEP2; Davis et al. 2003; Newman et al. 2013) in the Extended Growth Strip (EGS). Both spectroscopic surveys were obtained with the Keck/DEIMOS spectrograph (Faber et al. 2003) and the data were reduced with the same pipeline (Cooper et al. 2012).

Ancillary observations came from the Great Observatories Origins Deep Survey[14] (GOODS, Giavalisco et al. 2004), and the All-wavelength Extended Groth strip International Survey (AEGIS, Davis et al. 2007)[15]. As a reminder, stellar masses were calculated with UV-to-NIR SED fitting following the method described by Salim et al. (2007) when the photometry was available. Otherwise, stellar masses were estimated from the rest-frame K-band luminosity as described by J11 in their Appendix B. In GOODS-N, J11 used the following photometry: $UBVRIz$ taken from Capak et al. (2004) and JK obtained with the Flamingos camera on the Mayall 4 m NOAO telescope. For galaxies in EGS, they used FUV, NUV (GALEX), $ugriz$ (CFHTLS),

[11] All four classes (Star-Forming, Composite, LINER, and Sy2) are distinguished in the MEx classification software distributed on the world wide web in order to allow users flexibility in the choice of populations that they wish to consider or remove from their samples. IDL (Interactive Data Language) code and instructions are available here: https://sites.google.com/site/agndiagnostics/home/mex

[12] Subaru XMM Deep Survey/UKIDSS Ultra Deep Survey

[13] http://tkserver.keck.hawaii.edu/tksurvey/

[14] http://www.stsci.edu/science/goods/

[15] http://aegis.ucolick.org/

and K (Palomar) (see Salim et al. 2009; Gwyn 2008, 2011; Bundy et al. 2006). For EGS galaxies outside of the Canada-France-Hawaii Telescope Legacy Survey (CFHTLS) field-of-view, they used CFHT 12k BRI photometry (Coil et al. 2004).

Intermediate redshift galaxies are split into two redshift bins, $0.3 < z < 0.6$ and $0.6 < z < 1$, and are used only with the MEx diagnostic diagram because the redder lines [N II] and Hα are outside the observed range of those optical spectra at approximately $z > 0.4$. The parent galaxy sample and data are described by J11. For this work, galaxies were further selected to have S/N>3 emission line fluxes for [O III], while Hβ can be either a 3σ upper limit or a $> 3\sigma$ detection. As described by J11, Hβ fluxes were corrected for Balmer absorption using BC03 models to subtract the continuum when the spectra had a sufficient S/N per pixel (> 3) and otherwise using the median value of 2.8($\pm$0.9) Å. This correction changes the [O III]/Hβ ratios by 0.08 dex (r.m.s).

At $z > 1$, near-infrared spectra are required to measure rest-frame optical lines used for both the MEx and full BPT diagrams. Those were observed with Subaru/FMOS in SXDX/UDS (Y12), with a combination of HST/WFC3 and Keck/MOSFIRE in GOODS-S (T13), and with VLT/SINFONI or LBT/LUCI1 in the $z \sim 2$ sample (N14).

Ancillary data that were used in the work of Y12, T13 and N14 come from the Subaru XMM Deep Survey (SXDS, Furusawa et al. 2008) and UKIDSS Ultra Deep Survey (UDS, Lawrence et al. 2007) for the $z \sim 1.4$ sample, from the GOODS and CANDELS (Grogin et al. 2011; Koekemoer et al. 2011) surveys for the $z \sim 1.5$ sample, and from a more heterogeneous set of observations for the $z \sim 2$ sample. Detailed description of the latter can be found in the original SINS/zC-SINF survey descriptions (Förster Schreiber et al. 2009; Mancini et al. 2011) and in Sections 2.1 and 2.2 of N14.

The stellar masses and emission line ratios were taken from the published work introducing the samples (J11, T13, N14) or from private communication (K. Yabe, 2012). Information on each galaxy sample is summarized in Table 1. All three $z > 1$ galaxy samples were not corrected for stellar absorption. Y12 argue that it is negligible based on stellar population fitting around Hα (median correction of 4.2 Å is small compared to their typical Hα equivalent widths of 200 Å) and based on previous observations. Zahid et al. (2011) found a median value of 0.9 Å for Hβ from a stack of DEEP2 spectra at $0.75 < z < 0.82$, corresponding to a median shift downward by $\sim$0.03 dex. While the line ratios published by N14 do not include Balmer absorption, they have estimated that [O III]/Hβ would shift downward by $\sim$0.02 to 0.21 dex (mean of 0.08 dex) from their best fit SED-derived star-formation histories and ages.

Whenever available, multi-wavelength AGN classifications allow us to identify candidate AGNs independently from the emission line diagrams. These include X-rays in most cases (J11, T13, N14), as well as IRAC colors (Stern et al. 2005) and radio excess emission (Del Moro et al. 2013) for the $0.3 < z < 1$ galaxies, following the procedure described by Juneau et al. (2013). AGN identification by N14 also relied on other criteria including elevated emission line ratios in the central region of their spatially resolved emission line maps, or UV or mid-IR signatures (Förster Schreiber et al. 2009, Förster Schreiber et al., in prep.). On their side, Y12 excluded X-ray sources (Ueda et al. 2008) from their sample. The main characteristics of each galaxy sample are listed in Table 1.

3. REVISED MEX DIAGNOSTIC DIAGRAM

The MEx diagnostic diagram is revisited following two modifications relative to the initial design. First, the prior calibration sample is now built from SDSS DR7 instead of DR4. Second, the emission line signal-to-noise criterion is applied to the line ratios rather than to the individual lines (Section 2.1). Otherwise, the approach is very similar: we empirically determine dividing lines that follow transitional values of P(AGN), the probability of hosting an AGN according to the prior sample classified with the traditional BPT diagrams.

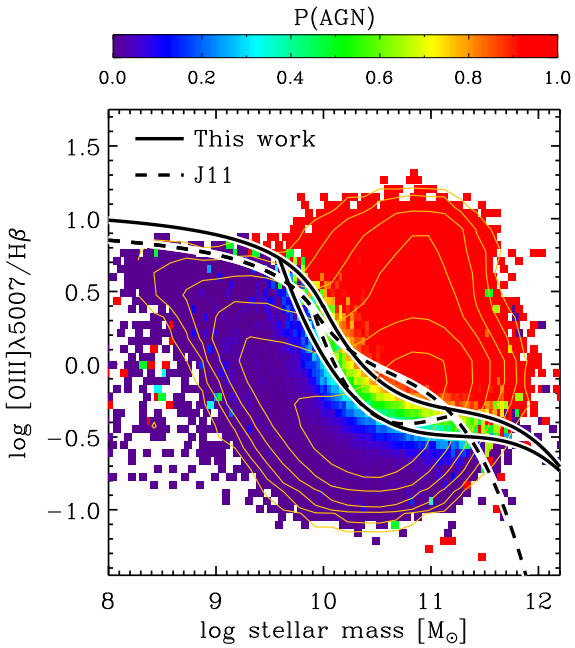

FIG. 1.— MEx diagnostic diagram for the SDSS DR7 emission-line sample at $0.04 < z < 0.2$. The contours mark the number density of galaxies in bins of 0.15 dex×0.15 dex, with the outermost contour corresponding to 10 galaxies per bin and a logarithm spacing in steps of 0.5 dex. The color scheme indicates the fraction of galaxies classified as AGN using the BPT-[N II] and [S II] diagnostics, from 0.0 (purple) to 1.0 (red). The demarcation lines are shown for the current sample (solid lines) as well as for the original MEx diagram built from SDSS DR4 by J11 (dashed lines).

At low stellar masses, the demarcation follows the upper envelope of the left-hand star-forming branch: $y = 0.375/(x-10.4)+1.14$, where $y \equiv \log([\text{O III}]\ \lambda5007/\text{H}\beta)$ and $x \equiv \log(M_\star)$. This relation is fixed but the value of the transition mass (M_{transi}), where the low-mass relation connects with the high-mass end, is left as a free parameter of the fit. At high stellar masses, a third order polynomial is adjusted to pass through regions with $0.6 < P(AGN) < 0.85$ for the upper MEx curve, and with $0.3 < P(AGN) < 0.5$ for the lower MEx curve[16].

[16] The ranges of $P(AGN)$ values were chosen to have a simi-

TABLE 1
Definition of Galaxy Samples

Sample	Number	Redshift	Flux Limit $\mathrm{erg\,s^{-1}\,cm^{-2}}$	Comments
$\langle z\rangle = 0.45$	1729	$0.3 < z < 0.6$	2×10^{-17}	GOODS-N and EGS fields (J11)
$\langle z\rangle = 0.7$	1662	$0.6 < z < 1.0$	2×10^{-17}	GOODS-N and EGS fields (J11)
$\langle z\rangle = 1.4$	32	$z\sim1.4$	4×10^{-17}	SXDS/UDS field (Y12)
$\langle z\rangle = 1.5$	36	$z\sim1.5$	3×10^{-17}	GOODS-S field (T13)
$\langle z\rangle = 2$	22	$z\sim1.5-2.5$	4×10^{-17}[a]	SINS/zC-SINF, GOODS-N and Q2343 fields (N14)

[a] The formal flux detection limit is not given by N14 but was estimated from the flux calibrated spectra shown in their article.
Columns: (1) Sample name; (2) Number of galaxies; (3) Redshift range; (4) 3σ Flux detection limit for emission lines; (5) Comments

Using the IDL package *mpfit* (Markwardt 2009) to solve for the best-fitting values, we obtain the following results.

The revised upper demarcation is defined as:

$$y = \begin{cases} 0.375/(x-10.5)+1.14 & \text{if x}\leq10 \\ a_0+a_1x+a_2x^2+a_3x^3 & \text{otherwise,} \end{cases} \quad (1)$$

where $y \equiv \log([\mathrm{O\ III}]\ \lambda5007/\mathrm{H}\beta)$ and $x \equiv \log(M_\star)$. The coefficients are the following: $\{a_0,a_1,a_2,a_3\} = \{410.24,-109.333,9.71731,-0.288244\}$. Similarly, the lower curve is given by the following:

$$y = \begin{cases} 0.375/(x-10.5)+1.14 & \text{if x}\leq9.6 \\ a_0+a_1x+a_2x^2+a_3x^3 & \text{otherwise.} \end{cases} \quad (2)$$

The coefficients are: $\{a_0,a_1,a_2,a_3\} = \{352.066,-93.8249,8.32651,-0.246416\}$.

We show the updated demarcations along with the original ones in Figure 1. The demarcations are mostly used for vizualisation purposes and the number of AGNs is instead calculated based on the underlying bivariate distribution of the prior galaxy sample. In this case, the $z\sim0$ SDSS DR7 emission-line sample (as defined in Section 2.1) is shown. When calculating a number – or fraction – of AGNs in a given galaxy sample, the use of AGN probabilities is more appriopriate than the strict use of the demarcation lines, and can yield to a smaller number of AGNs. This comes naturally from summing values of P(AGN)$\leq$ 1, but it should be kept in mind as it represents a difference from traditional use of AGN/SF diagnostic diagrams.

4. RESULTS

4.1. *Effect of Emission-Line Detection Limit*

Applications of the BPT-[N II] diagram at higher redshift must rely on NIR spectra with limited sensitivity (e.g. Shapley et al. 2005; Liu et al. 2008; Trump et al. 2013). In previous and current NIR spectroscopy studies, Hα and [O III] are the most commonly detected lines, while [N II] and/or Hβ are frequently undetected, yielding respectively to upper limits on [N II]/Hα or lower limits on [O III]/Hβ ratios. In what follows, we mimic such selection effects that arise within higher-redshift samples by requiring both Hα and [O III] in the $z\sim0$ SDSS sample to be more luminous than the emission line detection limits of intermediate to high-redshift optical and NIR spectroscopic surveys. There is no constraint applied to [N II] and Hβ to allow for cases that would have an upper limit only for either or both of those two lines.

In the low-redshift SDSS sample, the [O III] line tends to be less luminous than Hα in the majority (97%) of galaxies. This means that requiring both [O III] and Hα to be more luminous than a common threshold is effectively an [O III] selection at the 97% level. However, this trend only holds for 60-70% of galaxies for current samples of higher redshift galaxies (e.g., Ly et al. 2007; Colbert et al. 2013). For consistency across all redshifts considered in this work, we apply the line luminosity cut to both lines in the main part of this article, but we also consider various selections based on single emission lines or alternative line luminosity evolution in Appendix C. Some of the other scenarios yield similar results as there are more than one ways to select a comparison sample with better ressemblance to high-redshift galaxy surveys than using the full low-redshift SDSS survey as a comparison sample. The latter results in a poor comparison, and should therefore be avoided in many studies. We release versatile code allowing the user to apply different scenarios tailored to surveys probing rest-frame optical lines (Hβ and/or [O III] and/or Hα).

The first test consists of applying increasingly brighter luminosity cuts to Hα and [O III] for their inclusion in the sample. The results are respectively shown for the BPT-[N II] and MEx diagrams in Figures 2 and 3. As the emission line detection luminosity threshold increases, the bivariate distributions shift upward on both the BPT-[N II] and MEx diagrams. In other words, there is a bias against galaxies with low [O III]/Hβ ratio or with high [N II]/Hα when the latter is due to particularly weak Hα as occurs in LINERs and retired galaxies (Brinchmann et al. 2004; Cid Fernandes et al. 2011). The BPT demarcation lines appear to properly split the branches of the bivariate distributions in most cases. In details, the star-forming branch gets slightly closer to the Kauffmann line at the highest luminosity probed, suggesting a potential small shift toward higher [N II]/Hα and/or higher [O III]/Hβ, but this effect remains small (<0.2dex). However, the MEx demarcation lines no longer trace the morphology of the branches when a high luminosity threshold is applied. Instead, the location of the split between the two branches appears to shift toward higher stellar masses as the luminosity threshold increases (Figure 3). This shift arises because the MEx AGN probabilities (i.e., fraction of galaxies classified as BPT-AGN) depend on the emission line luminosi-

lar number of pixels to perform the fitting on the MEx plane for the upper and lower curve, and to bracket the intermediate region characterized by a steep gradient from $P(AGN)\sim0.3$ to $P(AGN)\sim0.85$; see color bar on Figure 1.

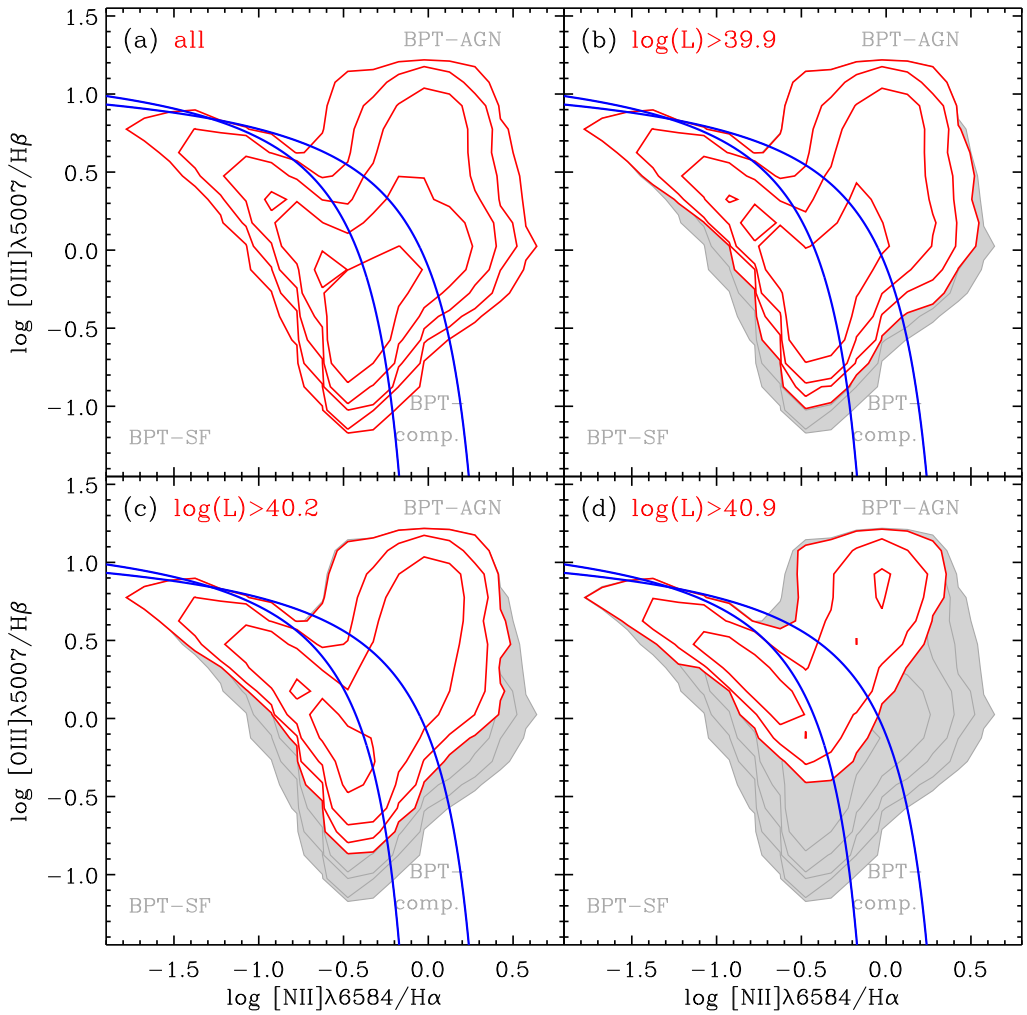

FIG. 2.— BPT-[N II] diagnostic diagram. The lower dividing line defines the upper envelope of star-forming galaxies (Kauffmann et al. 2003) while the upper line from Kewley et al. (2001) separates the most extreme AGN (above) from composite galaxies with a relatively higher SFR (between the lines). Red contours show the $z \sim 0$ SDSS sample with increasingly stricter luminosity thresholds applied to the Hα and [O III] lines: (a) no restriction, (b) $\log(L_{line}[\mathrm{erg\,s^{-1}}])> 39.9$ (c) $\log(L_{line}[\mathrm{erg\,s^{-1}}])> 40.2$, (d) $\log(L_{line}[\mathrm{erg\,s^{-1}}])> 40.9$. The underlying gray shaded contours show the full bivariate distribution identical to that in panel (a), and correspond to the number density per bin (0.15 dex×0.15 dex) with logarithmic spacing (0.5 dex). The outermost contour shows 10 galaxies per bin.

ties. Thus, we recalibrate the MEx diagram to take this dependence into account in the AGN probability calculations. We also calculate the corresponding offsets for the demarcation lines in Appendix B before reporting them on Figure 3.

4.2. *Emission-Line Diagnostics at Higher Redshift*

At moderate or high redshifts, galaxy samples may be subject to both emission line detection limits and evolution of the emission-line galaxy population as a whole. The former can be taken into account by applying the equivalent detection limit to the prior sample as described in Sections 4.1. If the low-redshift galaxy sample includes identical galaxies, applying the detection threshold should reproduce the properties of the higher redshift galaxies. However, this approach may fail if the low- and high-redshift samples are intrinsically different due to, e.g., significant evolution of the bulk of the galaxy population.

One form of evolution can be probed through emission line luminosity functions, which show a general fading of the emission-line galaxy population with cosmic time (e.g. Sobral et al. 2013; Colbert et al. 2013). In this work, we adopt an evolution of the characteristic luminosity given by $\log(L^*_{\mathrm{H}\alpha}(z)) = \log(L^*_{z=0} \times (1+z)^{2.27})$, obtained by fitting to a compilation of L^* values from the literature (Appendix C). We assume that the fading of the global galaxy population is traced by the fading of L^* and that by accounting for it, we select galaxies that have comparable line luminosities relative to the mean of the evolving population. In practice, this means that we compare high-redshift galaxies with lower redshift galaxies that have slightly less luminous emission lines.

We determine an effective minimum luminosity threshold to define the prior sample by using $L_{threshold} = L_{detection} - \Delta(L^*)$, where $\Delta(L^*)$ is the difference between L^* of the high-redshift sample and that of the comparison prior sample ($z = 0.09$). This fading may be explained by decreasing normalization of the $M_\star$−SFR main sequence with cosmic time (Noeske et al. 2007; Elbaz et al. 2007; Daddi et al. 2007; Elbaz et al. 2011), itself a consequence of a decreasing gas fraction in galaxies (e.g.,

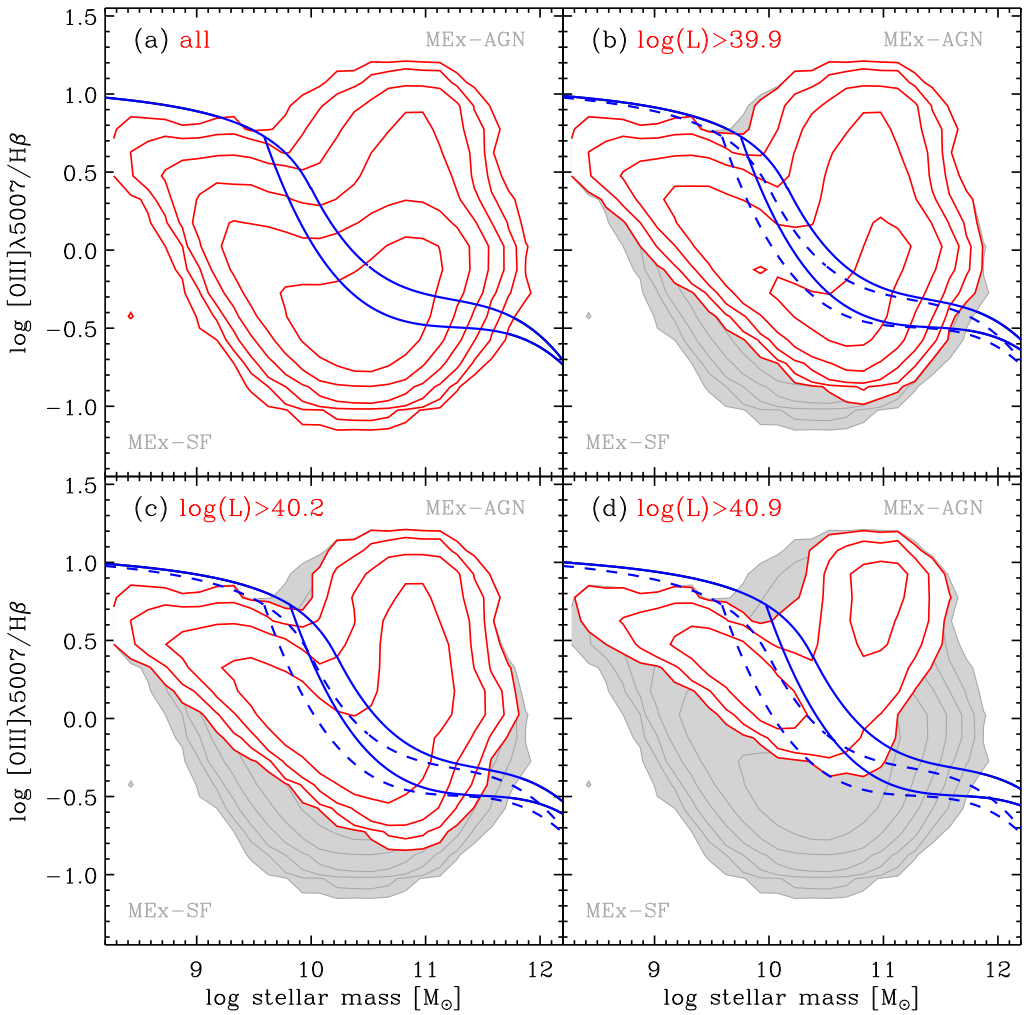

FIG. 3.— MEx diagnostic diagram. The dividing lines indicate regions corresponding to star-forming galaxies (below), MEx-intermediate galaxies (between) and MEx-AGN (above). The demarcation lines derived for the full sample are shown in panel (a) and in dashed lines in all other panels for reference. As in Figure 2, red contours show the distributions of $z \sim 0$ SDSS for varying line luminosity threshold (as labeled), while the gray shaded contours include the full $z \sim 0$ prior sample. Solid blue lines show the AGN/SF demarcations shifted following the AGN fractions calculated from the BPT classification (Appendix B).

Sargent et al. 2013). Regardless of the underlying cause, our motivation is to empirically choose galaxies at lower redshifts which are representative analogs of the higher-redshift population. In what follows, we make the assumption that the same evolution applies to both Hα and [O III] but different asumptions have also been implemented in this release of the MEx diagnostic code, as described in Appendix C.

It is possible that there is further evolution than fading of emission line luminosities associated with the decreasing star formation rates in galaxies. For instance, H II regions conditions may have been more extreme in the past, if struck by harder ionization fields and/or because of geometric constraints. Theoretical predictions have been recently developed by, e.g., Kewley et al. (2013a). We reserve discussion of these potential physical changes until Section 4.3, but we note that our approach empirically accounts for the observed evolution of the mass-metallicity relation (Section 5.1).

The intermediate and high redshift samples were described in Section 2.2, and the line flux limit for each survey is given in Table 1. For display purposes, we illustrate the prior sample corresponding to the line luminosity threshold at the median redshifts, i.e., the luminosity corresponding to the line flux detection limit minus the difference ΔL^* between the median redshift and that of the prior sample. The respective luminosity thresholds are $\log(L) > 39.9, 40.2, 40.9, 40.8, 41.1$ for the samples at $\langle z \rangle = 0.45, 0.7, 1.4, 1.5, 2$. An additional stellar mass limit is applied based on the minimum mass reached in each survey: $\log(M_\star[\mathrm{M}_\odot]) > 8.2, 8.6, 9.5, 9.0$ and 9.0 for the samples at $\langle z \rangle = 0.45, 0.7, 1.4, 1.5$ and 2, respectively. Combining this mass limit to the luminosity threshold, the prior samples can be used to predict the locus of higher-redshift galaxies on the BPT and MEx diagrams.

Figure 4 illustrates the results for two intermediate redshift slices, at $\langle z \rangle = 0.45$ and 0.7. The bulk of the points are located within the contours predicted through the combined line detection limit and L^* evolution. AGNs identified independently through diagnostics at other wavelengths (X-ray and/or IR) are highlighted. The

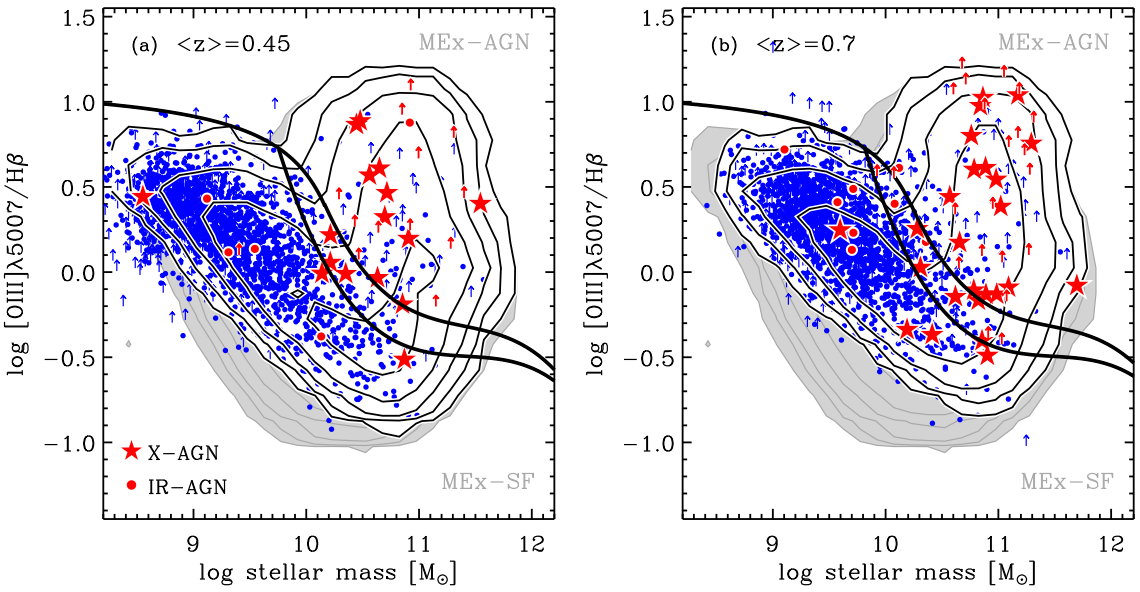

FIG. 4.— MEx AGN diagnostic diagram applied to intermediate redshift galaxies: (a) $\langle z \rangle = 0.45$, (b) $\langle z \rangle = 0.7$. The underlying gray shaded contours show the distribution of the full SDSS prior sample, while the black contours include the priors selected to match the detection luminosity threshold in each higher redshift subsample (including mild L^* evolution). The observed high redshift galaxies are shown with small filled circles, and highlighted with a large red circle (star) when there are known AGNs from mid-IR (X-ray). Lower limits on [O III]/Hβ are indicated with arrows, in red for mid-IR or X-ray AGNs, and in blue otherwise. The agreement between the predictions from the prior samples and the observed galaxies is generally good, especially with the X-ray AGN classification. The demarcation curves were calculated for the detection limit at the median redshift of each slice, and nicely separate the two branches seen in the contours and in the individual points. Contours are logarithmically spaced (0.5 dex) with the outermost contour corresponding to 10 galaxies per bin of 0.15 dex×0.15 dex.

agreement is especially good for AGNs thar are identified at least with X-ray signatures, with 81% (80%) lying in the MEx-intermediate or MEx-AGN regions at $z \sim 0.45$ ($z \sim 0.7$). When including [O III]/Hβ lower limits (red arrows), the agreement remains good with 86% (87%) at $z \sim 0.45$ ($z \sim 0.7$). However, there are more discrepancies with IR-only AGNs that are not also confirmed in X-rays (red circles). Only 1/5 at $z \sim 0.45$ and 1/6 at $z \sim 0.7$ lie in the MEx-intermediate or MEx-AGN regions. The remainder is located in the MEx star-forming region, which indicate that they are mis-identified in either the MEx or the IR diagnostic (mid-IR colors). Mid-IR color diagnostics are known to suffer from contamination by star-forming galaxies in the AGN regions when deep IRAC observations are used (Barmby et al. 2006; Donley et al. 2007, 2012), as is the case in this work. Therefore, it is possible that some IR-only candidates are not truly AGNs, but their number is small enough that the overall AGN classification is satisfactory (76% at $z \sim 0.45$ and 79% at $z \sim 0.7$). On the other hand, we do not expect to detect all MEx-AGNs with alternative methods as emission lines are the most sensitive probe and can reach much lower black hole accretion rates (Juneau et al. 2011, 2013).

At $z > 1$, we use three galaxy samples for which near-IR spectroscopy allows one to observe all the lines of the BPT-[N II] (Table 1). In each case, the same procedure is followed to empirically predict the loci of galaxies on both the BPT-[N II] and the MEx diagrams. The BPT -classification is also compared directly with that of the MEx diagram for the same galaxies.

The predictions from the SDSS priors appear suitable for the star forming branches of the BPT and MEx diagrams for both the $z \sim 1, 4$ and $z \sim 1.5$ samples (Figure 5). The observed points lie mostly within the predicted contours, especially if we consider that the sizeable error bars broaden the true distribution. We remind that all three $z > 1$ samples shown were not corrected for underlying Balmer absorption. Applying this correction would put their observed data points in slightly closer agreement with the predicted contours from SDSS galaxies by, e.g., shifting the points downward by ∼0.02 to 0.21 dex for the N14 sample (Section 2.2). The T13 sample has larger uncertainties due in part to a full Monte Carlo simulation of the continuum fitting that yield ∼ 30% larger error bars than the typical estimations, but also because low spectral resolution data were used for [O III]/Hβ ratios. Despite the larger individual uncertainties, the ensemble of points satisfactorily constrain the bivariate distribution of selected sample. Furthermore, when classifying individual galaxies on the BPT, we account for the uncertainties by marking cases which could be on either side of the Kauffmann et al. (2003) BPT dividing line as *uncertain*.

The two $z \sim 1.5$ samples behave slightly differently with respect to one another on the AGN side. Some of the differences can be attributed to selection as Y12 rejected X-ray AGNs from their parent sample. A few of the BPT-AGNs from the T13 work lie between the SF and AGN branches while some of the BPT-AGNs from the Y12 study are located low on the right-hand branch, but the latter are mostly lower limits on the [O III]/Hβ ratio, so they could still be fully consistent with the empirically predicted AGN branch.

The predictions for the $z \sim 2$ sample appear less consistent with the observations on the star-forming side of the diagrams. The $z \sim 2$ observations differ from both the $z \sim 1, 4$ and $z \sim 1.5$ samples. Perhaps $z > 2$ marks a

transition to strongly evolving ISM conditions in galaxies. However, it seems unlikely that there would be such a strong evolution during the 1 Gyr time span between $z = 2$ and $z = 1.5$, so the difference could instead be due to sample selection. One should keep in mind that the $z \sim 2$ sample was selected for spatially resolved spectroscopy, with preference given to high-mass galaxies: 67% (14/21) of galaxies have $M_\star > 10^{10.5}\ M_\odot$ in the N14 sample, while the corresponding fractions are 22% (8/36; T13) and 15% (4/27; Y12) for the $z \sim 1.5$ samples. Therefore, the N14 sample is substantially different from the other two. At such high stellar masses ($> 10^{10.5}\ M_\odot$), we predict that one needs to detect faint emission lines in order to probe star-forming galaxies. As can be seen in Figure 3, a luminosity threshold of $10^{40.2}$ erg s^{-1}still allows us to probe the star-forming branch on the MEx diagram, but this quickly vanishes as threshold line luminosities reaches $10^{40.3-40.4}$ erg s^{-1}. Therefore, one needs more than three times fainter fluxes than achieved by typical surveys at $z \sim 1.5-2$. In any case, given the various selection criteria and the small sample sizes, it is not surprising to see sample-to-sample variations. However, we can still conduct internal comparisons such as comparing the BPT and MEx diagrams for a given galaxy sample.

To this aim, Figure 5 is used to determine whether the BPT selection trends are analogous in the MEx diagram, and to compare the two AGN/SF classifications. The K03 dividing line is used on the BPT-[N II] in order to split BPT-AGN from BPT-SF galaxies. We incorporate information on the uncertainty of the classification for cases that overlap the dividing line when considering the measurement uncertainties (1σ error bars or limits). Ignoring the cases with uncertain BPT classifications, the MEx tend to slightly under-predict the number of AGNs relative to the BPT, especially at low masses ($< 10^{9.5-10}\ M_\odot$). On the other hand, there is virtually no contamination on the MEx-AGN side by BPT-SF galaxies in the $z \sim 1.5$ samples, and a few possible BPT-SF in the MEx-intermediate zone ($0.3 < P(AGN) < 0.7$) in the $z \sim 2$ sample. The number of $z \sim 2$ star-forming galaxies in the N14 sample is too low to confirm whether this trend is significant.

The fraction of galaxies with AGN according to the BPT and the MEx diagrams are listed in Table 2, where the MEx fraction is derived from the sum of AGN probabilities over the total number of galaxies. On the BPT, we compute both the fraction of the most secure AGNs (solid yellow circles), which corresponds to a lower limit on the true AGN fraction, and the fraction assuming that all points above the Kauffmann line have an AGN (open and filled yellow circles). In all cases, the 68% confidence interval on the fractions is given based on Bayesian binomial statistics using algorithms from Cameron (2011). The global AGN fractions from the MEx and BPT diagrams agree within the confidence intervals.

We furthermore indicate AGNs that are identified independently from the global emission line ratios (red symbols in Figure 5). All seven of these objects are securely classified as AGN on the MEx diagram, and lie above the Kauffmann et al. (2003) line on the BPT (three of them are formally in the BPT-composite region and the remaining four in the AGN region above the Kewley et al. (2001) line). Relative to the other BPT-AGNs, the independently classified AGNs (in red) tend to reside in more massive hosts. This was already observed at least for X-ray identified AGNs (e.g., Mullaney et al. 2012; Juneau et al. 2013). The bias toward high stellar mass hosts for X-ray AGNs may be due to a selection effect associated with the more limited sensitivity of X-ray observations and the higher likelihood to detect AGNs with lower Eddington ratios in galaxies hosting a more massive black holes, which themselves tend to be massive (Aird et al. 2012).

TABLE 2
Fraction of galaxies with AGN

Sample	MEx	BPT lower limit	BPT all AGN
$\langle z \rangle = 0.45$	0.29 ± 0.01	...	...
$\langle z \rangle = 0.7$	0.24 ± 0.01	...	...
$\langle z \rangle = 1.4$	$0.31^{+0.10}_{-0.07}$	$0.32^{+0.10}_{-0.07}$	$0.54^{+0.09}_{-0.09}$
$\langle z \rangle = 1.5$	$0.42^{+0.08}_{-0.07}$	$0.39^{+0.09}_{-0.07}$	$0.58^{+0.08}_{-0.08}$
$\langle z \rangle = 2$	$0.74^{+0.07}_{-0.11}$	$0.38^{+0.11}_{-0.09}$	$0.76^{+0.07}_{-0.11}$

Columns: (1) Sample name; (2) AGN fraction from the MEx diagram using AGN probabilities; (3) AGN fraction from the BPT for only the most secure AGN (filled yellow circles on Figure 5); (4) AGN fraction from the BPT using the Kauffmann dividing line.

The agreement between the BPT and the MEx diagrams is imperfect, with some BPT-AGNs lying on the MEx-SF side. This occurs for 3 (or 4) among 18 BPT-AGNs for the T13 sample, and 4 (or 6) among 9 BPT-AGNs for the Y12 not counting uncertain classes and either excluding (or including) the lower limits on [O III]/Hβ. This could be due to the greater sensitivity of the BPT, reaching much lower accretion rates, therefore probing intrinsically weaker systems relative to X-ray or IR observations. Indeed, as we pointed out, none of the X-ray identified AGNs are missed by the MEx diagnostic diagram. The presence of BPT-AGN in the MEx star-forming region may also reflect AGN incompleteness for hosts with low stellar masses ($< 10^{9.5-10}\ M_\odot$), or potential mis-classification on the BPT diagram if it evolved with redshift (Kewley et al. 2013a,b).

4.3. *Comparison with Theoretical Evolution Models*

Recently, Kewley et al. (2013a) presented a theoretical approach to predicting the location of higher-redshift galaxies on the BPT diagnostic diagram. Their framework is based on a description of two sequences on the BPT-[N II] diagram: an *abundance sequence* corresponding to the star-forming branch, and a *mixing sequence* where the AGN contribution to the emission lines rises toward the upper right part of the diagram. Kewley et al. (2013a) use the photoionization code MAPPINGS IV (Dopita et al. 2013) with input Starburst99 stellar population models radiating on ISM with varying metallicities to define the abundance sequence. The AGN contribution is added with emission lines from dusty Narrow-line region (NLR) models calculated with MAPPINGS III as described by Groves et al. (2004). An increasing AGN contribution forms the mixing sequence[17].

[17] Kewley et al. (2013a) also explored slow shock models and found them to predict line ratios that are distinct from those produced by AGN photoionization (their Section 5.1).

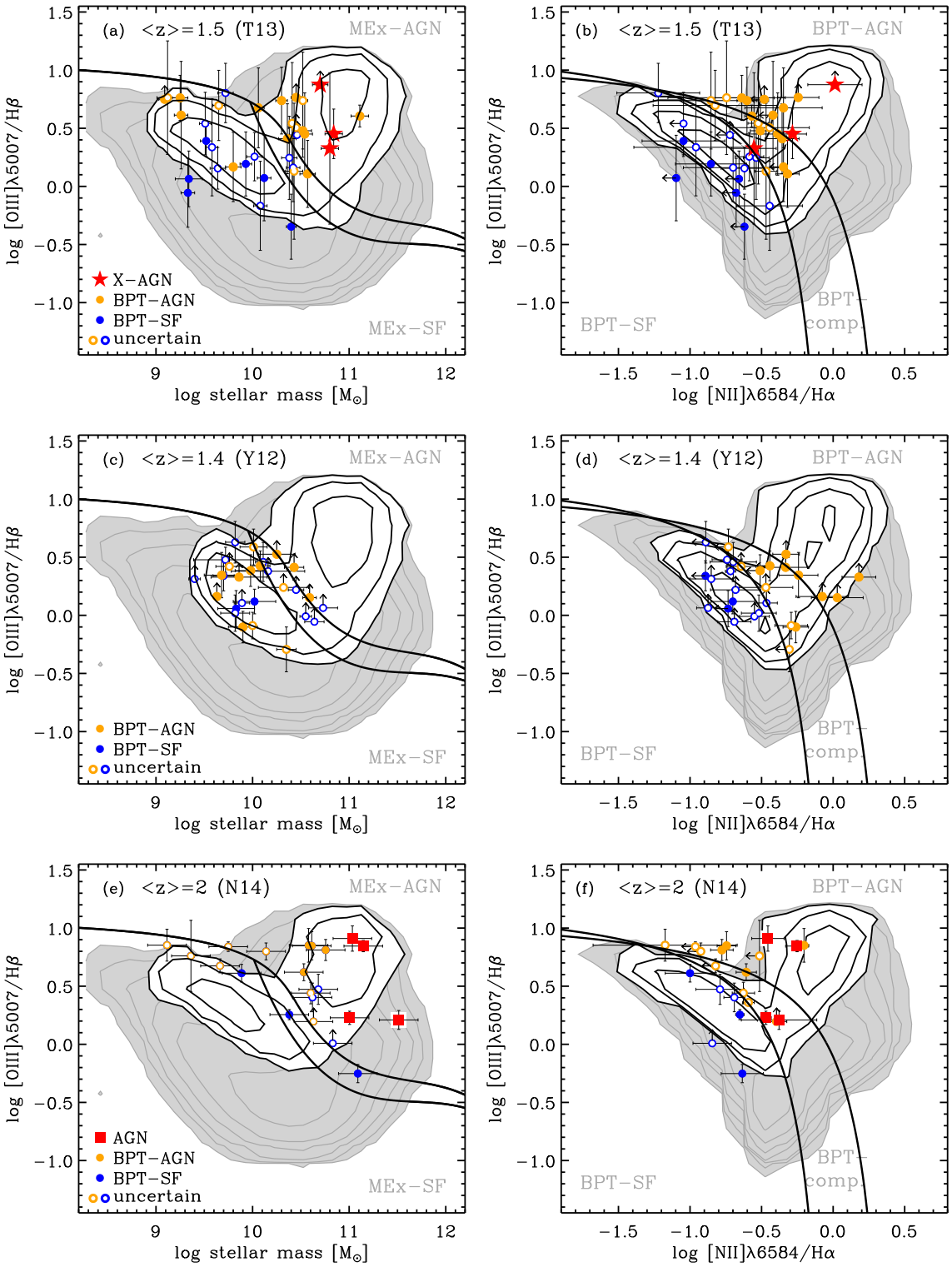

FIG. 5.— AGN diagnostic diagrams applied to high redshift galaxies ($z \sim 1.5-2$). Three samples are shown (one per row). In each row, the MEx is on the left-hand side (panels a, c, e) while the BPT for the same galaxies is on the right-hand side (panels b, d, f). The top row illustrates the T13 sample at $z \sim 1.5$, noting that X-ray identified AGNs are marked with red star symbols, and that points are otherwise color-coded according to the BPT classes as labeled. The uncertain classes denote points which could be on either side of the Kauffmann line when accounting for the error bars (open circles). The second row shows the sample of Y12, with the same color coding except that X-ray AGNs were discarded from their parent sample. The third row shows the sample of N14 with AGNs identified independently in red (from spatially-resolved line ratios or from X-ray, UV, or mid-IR). In all panels, the underlying gray shaded contours show the distribution of $z \sim 0$ emission-line SDSS sample, while the black contours include the SDSS subsample selected to match the detection luminosity threshold in each higher redshift subsample (including the simple L^* evolution). Contours are logarithmically spaced (0.5 dex) with the outermost contour corresponding to 10 galaxies per bin of 0.15 dex×0.15 dex.

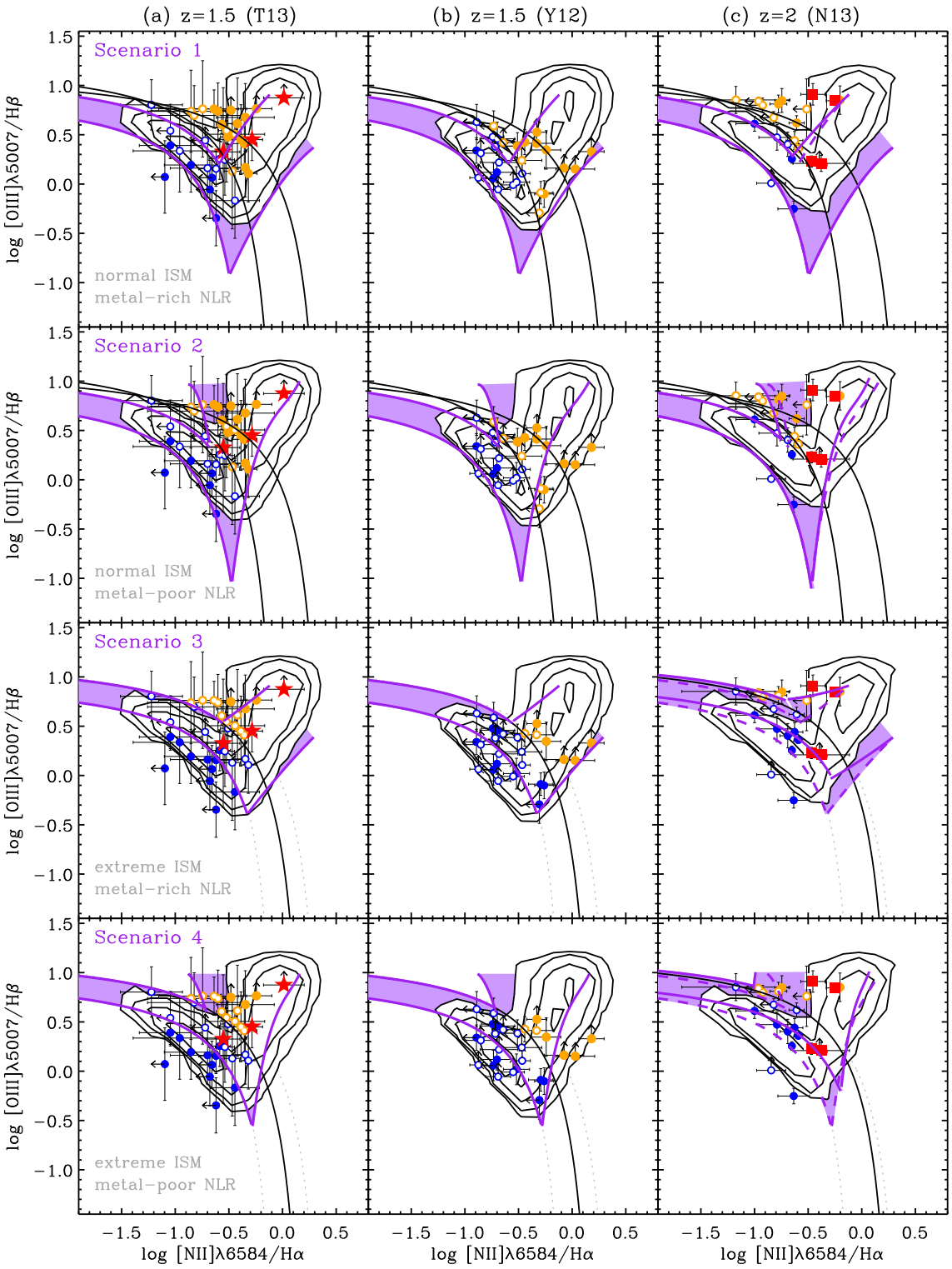

FIG. 6.— BPT-[N II] diagrams for the three $z > 1$ samples, in columns (a), (b), and (c), as labeled. The SDSS-based empirical predictions (black contours) are compared with the theoretical predictions of the scenarios from Kewley et al. (2013a) (purple regions). Each row corresponds to a scenario from 1 (top) to 4 (bottom), each with different assumptions for the evolution in ISM conditions and NLR metallicity. For the $z \sim 2$ sample, the evolutionary trends are shown at $z = 1.5$ (dashed lines) and $z = 2.5$ (solid lines), bracketing the redshift range of the observations. Plotting symbols are identical to Figure 5. Contours are logarithmically spaced (0.5 dex) with the outermost contour corresponding to 10 galaxies per bin of 0.15 dex×0.15 dex.

Kewley and collaborators explored four different evolutionary scenarios:

1. Normal ISM and metal-rich AGN NLR at high z
2. Normal ISM and metal-poor AGN NLR at high z
3. Extreme ISM and metal-rich AGN NLR at high z
4. Extreme ISM and metal-poor AGN NLR at high z

In the first two cases, the abundance sequence remains unchanged with redshift. Purely star-forming galaxies are predicted to move along the sequence as their gas-phase metallicity evolves. According to the last two scenarios, star-forming galaxies have more extreme ISM conditions, with a higher ionization parameter, higher electron densities, higher star formation surface densities or a combination. In these cases, the locus of the abundance sequence shifts toward higher [O III]/Hβ at higher redshifts.

For each set of ISM conditions, there are two alternative scenarios for the abundance of the AGN NLRs. The NLR gas is assumed to either be enriched early, meaning that the NLRs are metal-rich across the full range of redshifts considered, or to have a gas-phase abundance that changes with cosmic time following the evolution of the $M_\star - Z$ relation for star-forming galaxies. A lower NLR metallicity yields to lower [N II]/Hα ratios (Groves et al. 2006), and therefore changes the mixing sequence. These four scenarios are compared to observations of galaxies at intermediate to high redshifts by Kewley et al. (2013b).

Figure 6 illustrates a comparison between our empirical approach and the four scenarios developed by K13, applied at $z > 1$. At first glance, the $z \sim 0$ empirical predictions (black contours) appear intermediate between scenarios 1 and 2, with normal ISM conditions. However, an important distinction is that the empirical method predicts the absence of galaxies with comparatively low [O III]/Hβ for the high redshift samples, due to line luminosity detection threshold. In their initial comparison with observations, Kewley et al. (2013b) have not included selection effects caused by the non-detection of intrinsically faint lines at higher redshifts. Including those effects would namely trim the region predicted to reach low [O III]/Hβ values according to Scenarios 1 and 2, thus increasing the lower envelopes of the K13 models with normal ISM conditions.

If the empirical predictions from the selected $z \sim 0$ SDSS subsamples favor Scenarios 1 and 2, what is the preferred scenario according to the observed high-redshift galaxies? Because of the large sample-to-sample variation between the observations, it is not obvious what scenario is prefered (Figure 6). On the star-forming side, both the $z \sim 1.4$ and $z \sim 1.5$ samples are fully consistent with the empirical predictions from the matched $z \sim 0$ galaxies. Therefore, the locus of those $z \sim 1.5$ galaxies is better represented by normal ISM conditions (with selection effects) rather than the strong ISM evolution of some of the K13 models (scenarios 3 and 4). The case of the N14 sample is less clear because of the dearth of low and moderate mass galaxies (Figure 5), and therefore the predicted small number of star-forming galaxies in that sample (Section 4.2). It remains possible that this sample favors a more strongly evolving ISM at $z > 2$, which could be supported by even higher redshift results at $z \sim 3$ (e.g., Holden et al. 2014).

Regarding the AGN branch, the T13 and N14 samples (columns a and c of Figure 6) appear to be better represented with metal-poor NLR on the AGN side (Scenarios 2 and 4). The Y12 sample lies between the predictions from metal-poor and metal-rich NLRs, but also includes lower limits on [O III]/Hβ, which prevent us from knowing the true distribution of the small number of AGNs. We also recall that Y12 excluded AGNs that were a priori identified from their parent sample, and so this sample provide us with a less stringent contraint on the AGN side. Overall, the $z \sim 1.5$ data may favor Scenario 2, with normal ISM in galaxies and metal-poor NLRs at higher redshifts, although we note that larger samples are needed to confirm this conclusion, and whether there is a transition to stronger ISM evolution at $z > 2$.

5. DISCUSSION

5.1. *Mass-Metallicity Relation*

Several studies have reported evolution of the stellar mass-metallicity (MZ) relation for galaxies (Savaglio et al. 2005; Erb et al. 2006; Zahid et al. 2013a), or along a plane in the $M_* - SFR - Z$ space (Mannucci et al. 2010; Lara-López et al. 2010; Yates et al. 2012). There are variations in the details of this evolution and how it may vary with galaxy stellar masses, but the general sense is that at a given stellar mass, lower redshift galaxies have higher gas-phase metallicities than their higher redshift counterparts. This could indicate the global enrichment in galaxies as they evolve and form stars.

The revised MEx demarcations and probabilities now include metallicity evolution indirectly through the use of line luminosities to build a prior sample. As we show below, together with the stellar mass, emission line luminosities can trace metallicity to some extent. This is similar, though not identical, to previous work defining the Fundamental Metallicity Relation (Mannucci et al. 2010; Lara-López et al. 2010; Yates et al. 2012; Cresci et al. 2012). In the latter, the SFR is used as a third parameter to define a plane while here we use both Hα luminosity, a tracer of the SFR (Kennicutt 1998), and [O III], which depends more directly on the gas-phase metallicity. We also *fade* the line luminosity threshold by the corresponding fading of the knee of the Hα luminosity function.

We test directly our selection method against observed MZ relations compiled by Zahid et al. (2013a, hereafter Z13). These authors fitted the functional form defined by Moustakas et al. (2011) to datasets in five redshift slices, including an intermediate-redshift DEEP2 sample ($z \sim 0.8$), and the Y12 sample ($z \sim 1.4$), which overlap with the present study. These MZ relations are compared to our empirical predictions from SDSS prior samples. We compute metallicities following the same method as Z13 to facilitate a direct comparison. As in that study, we apply the KK04 calibration Kobulnicky & Kewley (2004) to the required [O II], Hβ, and [O III] emission lines. Line fluxes were first corrected for dust attenuation by measuring the Balmer decrement and applying the Calzetti et al. (2000) dust attenuation curve with $R_V = 4.05$, assuming an intrinsic ratio of Hα/Hβ=2.86 (Osterbrock & Ferland 2006).

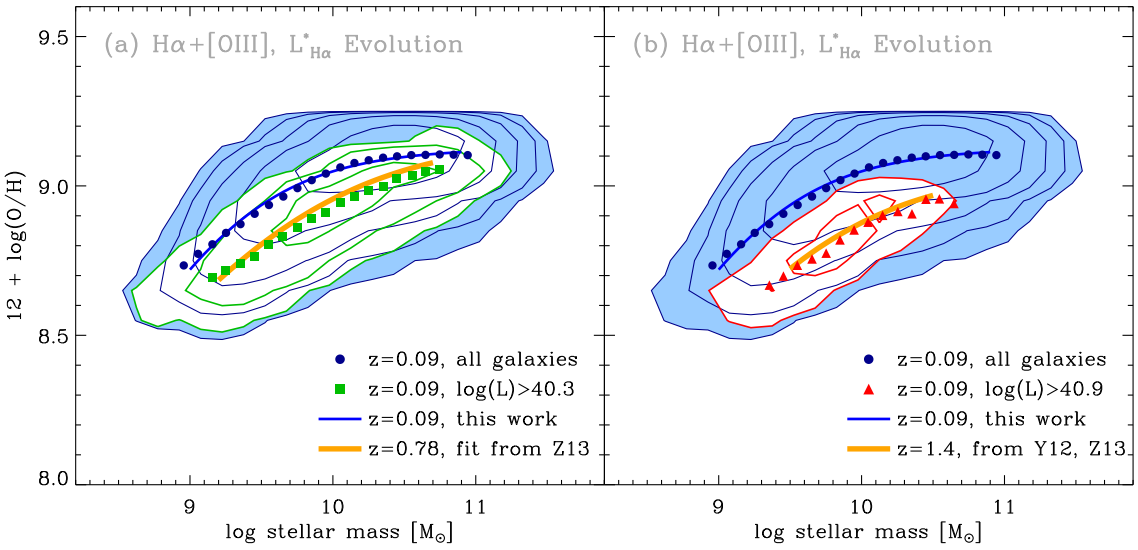

FIG. 7.— MZ relation from SDSS observations at low-redshift (this work) and from observations compiled by Zahid et al. (2013a), who fitted DEEP2 $z \sim 0.8$ and Y12 $z \sim 1.4$ results (thick orange curves). In all panels, the blue logarithmically-spaced contours show the full SDSS prior galaxy sample, with filled circles marking the median metallicity in stellar mass bins of 0.1 dex. The blue line shows the fitted relation using the functional form introduced by Moustakas et al. (2011). Green and red contours correspond to a SDSS subsample with Hα and [O III] lines above the labeled luminosity. The median metallicity in stellar mass bins of 0.1 dex is shown with filled symbols. The choice of the threshold luminosity is made according to the fiducial scenarios, where the luminosity detectability threshold is lowered by the same amount as L^*(Hα) fades between the redshifts of interest: (a) $z \sim 0.8$ and (b) $z \sim 1.4$, and the prior sample at $z \sim 0.09$. In this case, the predicted contours and median values agree remarkably well with the observed relations compiled by Z13. Alternative scenarios and more details are included in Appendix C. Contours are logarithmically spaced (0.5 dex) with the outermost contour corresponding to 50 galaxies per bin of 0.15 dex×0.15 dex.

In Figure 7, we show predicted contours using our fiducial approach (Hα and [O III] selection above the luminosity threshold that includes $L^*_{\rm H\alpha}$ evolution). There is a good global agreement between predicted contours and analytical fits to observations reported by Z13, indicating that the observed MZ evolution is a built-in feature of our method. Empirical predictions were also made for two alternative scenarios (Appendix C), namely to compare with samples selected from a single line: [O III] or Hα, but also to consider null evolution scenarios where the line luminosity detection limits are used as is.

We note that the empirical prediction of the Y12 sample (red contours on panel b) show a cutoff at high masses ($> 10^{10.5}\ M_\odot$). While galaxies with these high masses and low metallicities may be more common at higher redshifts. This is likely a true evolutionary trend, and could indicate that most massive galaxies have had time to enrich their ISM by $z < 0.2$ and that the galaxies that remain with low metallicities at this more recent epoch have lower stellar masses.

5.2. *Is there evolution in the emission-line diagnostics?*

In Section 4.1, we investigated the consequences of increasing emission-line luminosity limits to select subsamples from $z \sim 0$ SDSS emission-line galaxies, and the resulting bivariate distributions on the BPT and MEx diagrams. We found that the division line developed by Kauffmann et al. (2003) still appears to be applicable to divide the two branches defined by the data at all the luminosity thresholds tested, albeit a small shift of <0.2dex toward higher [N II]/Hα and/or [O III]/Hβ could be possible at the highest line luminosities. This suggests that the luminosity dependence would more strongly affect the locus of the sample than the definition of the dividing lines. In Section 4.2, we compared $z \sim 1.5 - 2.5$ observations with empirical predictions from SDSS subsamples selected to have equivalent line luminosity limits. We found a general but imperfect agreement between the observations and matched SDSS prior samples on the BPT diagrams. Namely, some galaxies from the T13 and N14 samples are located between the two empirically predicted BPT branches on the right-hand side panels of Figure 5. This feature could be due to lower NLR metallicity, such as predicted by K13 with their Scenario 2 (second row of Figure 6). Alternatively, it could be due to AGN host having higher SFRs at higher redshifts, which would boost Hα more strongly than [N II] and dilute the AGN signatures.

Lower NLR metallicites and/or higher SFRs at higher redshift imply a potentially greater fraction of AGNs in the BPT-composite region (between the Kauffmann et al. 2003 and Kewley et al. 2001 lines) and even toward the top of the star-forming branch. This trend could explain the presence of X-ray (or otherwise securely-identified) AGNs on the boundary between the composite and star-forming regions of the BPT-[N II] diagram in the T13 and N14 samples (red symbols in Figure 5) and the presence of data points to the left of the AGN branch on the BPT diagram. As a consequence, AGN samples should include BPT-composites to improve their completeness (also see Trouille et al. 2011). Conversely, purely star-forming galaxy samples may be harder to obtain given the higher risk of including AGN contaminants when NLR metallicities are lower. A potential solution may be to combine both the BPT and MEx classification schemes in such ambiguous cases.

How do these trends compare on the MEx diagram? In contrast to the BPT diagram, the splitting of the two

branches traced by $z \sim 0$ SDSS samples on the MEx diagram shows an obvious offset with increasing line luminosity limits (Figure 3). This offset corresponds to changes in the AGN probabilities as a function of line luminosity limits, with the transition region shifting toward higher stellar masses with increasing line luminosity limits (fitted in Appendix B). The physical interpretation depends on the nature of the main ionizing source. For purely star-forming galaxies, brighter lines correspond to lower metallicity and/or higher SFRs, and therefore higher [O III]/Hβ ratios.

However, on the AGN side, brighter lines imply higher accretion rates onto black holes (traced by [O III]) as well as higher SFR of the hosts (traced by Hα). Both of these criteria will favor high-mass hosts. First, massive galaxies are more likely to host high-mass black holes (e.g. Magorrian et al. 1998; Gebhardt et al. 2000; Ferrarese & Merritt 2000), which will be brighter than lower mass black holes for a given Eddington ratio distribution (also see Aird et al. 2012). Second, high mass galaxies are more likely to have high SFRs, according to the M_*-SFR sequence for star-forming galaxies[18] (Brinchmann et al. 2004; Noeske et al. 2007; Elbaz et al. 2011). Therefore, these trends likely combine to shift the star-forming galaxies/AGN division toward higher stellar masses. Regardless of the underlying interpretation, the empirical offset has been calibrated, allowing one to trace the MEx demarcation lines for various line sensitivity limits. The MEx AGN probabilities can be calculated taking into account both the survey detection limit, and the individual redshift of each galaxy (which will determine the amount of L^* evolution).

While the $z > 1$ samples on the BPT diagram suggested offsets of AGN NLRs toward lower metallicities (i.e., lower [N II]/Hα ratios), the MEx diagram is largely insensitive to such an effect, as the [O III]/Hβ would vary in the opposite direction, *helping* the AGN selection. Instead, the MEx diagnostic has the caveat of being incomplete to select AGNs at low stellar masses ($< 10^{9.5-10}$ $M_\odot$). This limitation depends slightly on line luminosities with this new approach (galaxies with more luminous emission liness can only be recognized as AGNs in higher mass hosts relative to galaxies with fainter lines). This limitation may not be very severe if AGNs in low-mass hosts are rare (Bellovary et al. 2011; Tanaka 2012), and/or if their relative importance was lower at higher redshift, as would be the case if AGN activity followed the downsizing phenomenon (e.g., Barger et al. 2005; Kelly & Shen 2013; Hirschmann et al. 2013). The situation is different if one is particularly interested in low-mass AGN hosts, low-mass black holes and black hole seeds (Greene & Ho 2007; Barth et al. 2008; Díaz Tello et al. 2013; Reines et al. 2013).

5.3. *Lower NLR metallicity at higher redshifts: gas-poor hosts or metal dilution?*

NLRs tend to be metal-rich in nearby galaxies, and while there is evidence for low-metallicity AGNs, those systems are rare (Groves et al. 2006). In this study, we find tentative evidence that higher redshift AGNs may be less chemically enriched than their local counterparts. We discuss a few physical mechanisms that could explain this trend, in light of our recent understanding of high-redshift star-forming galaxies.

As also mentioned by Kewley et al. (2013a), emission lines from NLRs may trace gas closer to galaxy nuclei than global galaxy-scale spectra. Negative metallicity gradients could therefore play a role in explaining that NLRs are typically more metal-rich than the surrounding galaxy ISM at larger scales. In this view, if disk galaxies start with flatter gradients at higher redshifts, the NRLs in these hosts would also exhibit more metal-poor characteristics. Conversely, if the nuclei of galaxies enrich on very short timescales, then the NLRs would be metal-rich already in higher redshift systems, meaning that their hosts had steeper metallicity gradients. Thus, NLR metallicities could trace whether host galaxies have had time to enrich at least their central regions, and whether disks grow inside-out (e.g., Jones et al. 2013). However, this simple picture may not hold during galaxy mergers because metal-rich nuclei could be diluted by inflows of more pristine gas brought in from the outskirts or from satellite galaxies. Galaxy mergers and interactions have indeed been reported to exhibit flattened or inverted metallicity gradients (e.g. Kewley et al. 2010; Rupke et al. 2010; Queyrel et al. 2012), though major merger events only account for a small fraction of the total star-forming and AGN galaxy population at a given time.

Here, we discuss one more possibility related to violent disk instabilities (VDIs; e.g., Bournaud et al. 2007; Dekel et al. 2009). High-redshift disk galaxies have been observed to have high gas fractions at $z > 1.5$ (Daddi et al. 2010; Tacconi et al. 2010), and clumpy appearances (e.g. Elmegreen et al. 2007, 2009) that distinguish them from typical star-forming disk galaxies observed at low redshifts, and that are interpreted as observational signatures of VDIs. These instabilities are predicted to be ubiquitous at $z > 1-2$, and to generate inflows toward the central regions (Krumholz & Burkert 2010; Bournaud et al. 2011). These inflows can bring metal-poor gas in the viscinity of active BHs and result in lower metallicity NLRs. While VDI clumps are themselves star-forming and produce metals, they undergo outflows (Genzel et al. 2011) as they migrate inwards but also accrete gas from their diffuse surrounding (Dekel & Krumholz 2013; Bournaud et al. 2014). This could potentially maintain somewhat lower metallicities for these clumps, or the general turbulence could contribute to erase or flatten metallicity gradients (e.g., Queyrel et al. 2012, for an example case). The details and timescales are still uncertain, but we speculate that VDIs could play a role in determining the observed metallicities of NLR gas at higher redshifts ($z > 1$).

5.4. *Comparison with previous MEx diagram results*

In this work, we have revised the MEx demarcation and probability calculations to use the SDSS DR7 sample (Section 3). We have then implemented changing MEx demarcation and probabilities as a function of the effective luminosity threshold for emission line detection (applied to Hα and [O III]). How do these revisions com-

[18] The emission line selection will favor star-forming or active galaxies over truly passive systems which do not follow the M_*-SFR sequence. This bias will be increasingly important as the emission line luminosity limit increases, therefore increasing the likelihood that the selected galaxies are star-forming and not passive.

pare to other studies of the MEx at high-redshift from the literature?

On the one hand, T13 had found a good agreement between the BPT classification and the original MEx dividing curves from J11, and concluded that the original MEx classification were valid for their sample at $z \sim 1.5$. The revised demarcations are now shifted slightly upwards at low masses based on the low-redshift calibration with SDSS DR7 (Figure 1). This feature increases the number of low-mass BPT-AGNs that lie in the MEx-SF region at the top left of the star-forming branch and slightly worsens the agreement.

On the other hand, N14 noted that the original MEx demarcations should be displaced to higher stellar masses in order to improve the agreement between the BPT and MEx diagrams at $z \sim 2$. In this case, our revised MEx dividing curves improve the agreement and mitigate the need for such a large shift. Instead, the revised MEx demarcation lines introduced here appear to be applicable out to $z \sim 2$ given the current observational constraints, and given the limitations of the uncertain BPT classes for galaxies with measurement errors spanning the AGN/SF demarcation, which were not taken into account by N14. More recently, Henry et al. (2013) also suggested that the MEx demarcation should shift to higher stellar masses at higher redshifts, and suggested a 1 dex shift for their galaxy sample at $1.3 < z < 2.3$.

The empirical approach presented in this Paper lies between these two conclusions, i.e., it includes a line luminosity dependence that mimic high-redshift galaxies on line ratio diagnostics, and accounts for MZ relation evolution (Section 5.1) but the mass offsets on the MEx doagnostic diagram are generally not as extreme as those suggested by N14 and Henry et al. (2013). A direct consequence of using the revised MEx diagnostic at higher redshifts will be to yield slightly lower AGN fractions compared to the original J11 version. This was noted by Mignoli et al. (2013) in their work comparing AGNs identified from [Ne V] λ3525 and X-rays in zCOSMOS, with the MEx diagnostic among others.

The MEx demarcation lines can be further tested in future investigations by using the publically available MEx probability calculation code[19], with optional emission line detection limits tailored to each survey, and with or without prescriptions for L^* evolution to the redshift of each individual galaxy. It will also be informative to push the analysis to yet higher redshift, with new samples becoming available (e.g. Holden et al. 2014), which will be a follow-up work to this article.

In Appendix D, we present a example application to intermediate-redshift ($0.2 < z < 0.8$) galaxy samples from the stacked spectral analysis of Vitale et al. (2013). We have also implemented alternative selections based on a single emission line, Hα or [O III], in the public distribution of the code (Appendix C).

6. SUMMARY

Galaxies at higher redshifts appear offset from the locus of low-redshift galaxies on emission-line diagnostic diagrams such as the BPT and MEx diagrams. These two planes share a common vertical axis and behave similarly but with noticeable differences. In this Paper, we have investigated the cause of this apparent redshift-dependent offset, improved the applicability of the MEx diagram to a range of redshifts, and demonstrated the crucial importance of taking into account selection effects due to emission line detection limits.

Our main results are:

1. We have revised the $z \sim 0$ demarcations of the MEx diagnostic diagram with a $0.04 < z < 0.2$ prior sample of emission-line galaxies selected from SDSS DR7, a superset of the SDSS DR4 sample that was used in the original definition of the MEx by J11.

2. Imposing a minimum line luminosity to Hα and [O III] λ5007 affects the bivariate distribution of the galaxies on the BPT and MEx diagrams. With increasing line luminosity, the shift is in the sense of higher [O III]/Hβ ratios in both cases (Figures 2 and 3), and toward lower [N II]/Hα for the AGN branch of the BPT. Therefore, we find that selection effects applied to $z \sim 0$ samples mimics the high values of [O III]/Hβ, and (among AGN) comparatively lower [N II]/Hα ratios seen in galaxy samples at $z > 1$.

3. In the case of the MEx diagram, the splitting between the star-forming branch and AGN branch – where the SF/AGN classification comes from the BPT diagram – occurs at increasingly higher stellar mass as the cutoff line luminosity is raised. We thus develop a line detection-limit dependent MEx diagnostic diagram.

4. At $z < 1$, optical spectra of ∼3400 galaxies with [O III] and Hβ are used on the MEx diagram. The line luminosity threshold was calculated in two redshift slices, $0.3 < z < 0.6$ and $0.6 < z < 1$, using the formal flux detection limit of the surveys, corrected for a mild luminosity evolution of the population ($L^*_{\rm H\alpha}$ evolution). These luminosity limits of 10^{40} and $10^{40.4}$ erg s^{-1}empirically predict the locus of these respective sample on the MEx diagram (Figure 4).

5. At $z \sim 1.5 - 2$, we gather three published galaxy samples with near-IR spectroscopy for which all four BPT lines are covered, enabling us to apply both the BPT and MEx diagnostics (Figure 5). The prior samples predict well the allowed region on the diagrams, without invoking evolving H II conditions out to $z \sim 1.5$. The case at $z \sim 2$ is less clear due to small sample size, a high fraction of massive ($> 10^{10.5}$ $M_\odot$) galaxies, and ambiguous classification on the BPT diagram (conflicting classes when accounting for line ratio uncertainties).

6. A comparison with theoretical predictions by Kewley et al. (2013a) and observations at $z \sim 1.5$ suggests that the favored scenario for star-forming galaxies may be *normal* H II region conditions when one also accounts for selection effects. The latter tend to prevent the detection of galaxies with low [O III]/Hβ ratios. There may be transition at $z > 2$

[19] https://sites.google.com/site/agndiagnostics/home/mex

toward more strongly evolving ISM conditions but future work is needed to confirm this possibility.

7. On the AGN side, the data appear to favor K13 scenarios with varying metallicity of narrow-line regions photoionized by AGN, with lower metallicities at higher redshifts. The observed sample-to-sample variation at $z > 1$, and the sizeable error bars, do not allow us to firmly rule out the metal-rich NLR scenario.

8. Selecting emission lines based on detectability at higher redshifts allow us to reproduce remarkably well the observed evolution of the MZ relation (Figure 7). Thanks to this feature, the locii of prior SDSS samples on the MEx diagram and associated AGN probabilties include this reported MZ evolution. We find that the slope and/or offset of observed MZ relations may depend on sample selection and emission-line detection limits (Figure 14).

9. In addition to a fiducial method where we require both [O III] and Hα lines to be above a common threshold luminosity, we also implement selection and evolution scenarios based on a single emission line and/or based on different evolutionary schemes (including a null evolution; Appendix C). These scenarios can offer a better description of observed high-redshift samples than using the full SDSS sample, and generally stress the importance of accounting for sensitivity limits in emission-line studies.

Larger galaxy samples with a well-understood selection function and deep spectral coverage are required to better disentangle between ISM evolutionary scenarios. However, when such samples are available, care should be taken to include selection effects in order to avoid ruling out a scenario based on the absence of observed galaxies in a region that is beyond the detectable limit, such as low [O III]/Hβ ratios on AGN diagnostic diagrams, and correspondingly a high gas-phase metallicities for galaxy abundance surveys relying on [O III] detection. Properly accounting for selection bias will be crucial to unravel the underlying physics explaining the locus of galaxies on nebular line diagrams. The empirical approach and publicly available code presented here should be applicable to future medium and large-scale NIR spectroscopic surveys, with facilities such as Magellan/MMIRS, Keck/MOSFIRE, Subaru/FMOS, VLT/KMOS, Gemini/Flamingos-2, and JWST/NIRSpec as well as Euclid.

The authors thank the anonymous referee for comments that greatly improved this article, and that motivated the development of a much more versatile tool. The authors also thank K. Yabe for kindly sharing the stellar masses and line ratios for their galaxy sample (Yabe et al. 2012), and M. Vitale for generously sharing their stacked spectra results (Vitale et al. 2013). SJ would like to acknowledge useful discussions with L. Kewley, M. Mignoli, G. Cresci, M. Brusa, and M. Sarzi as well as earlier discussions with C. Scarlata and H. Teplitz. SJ and FB acknowledge support from the EU through grant ERC-StG-257720. SC acknowledges support from the European Research Council via an Advanced Grant under grant agreement no. 321323.

Funding for the SDSS and SDSS-II has been provided by the Alfred P. Sloan Foundation, the Participating Institutions, the National Science Foundation, the U.S. Department of Energy, the National Aeronautics and Space Administration, the Japanese Monbukagakusho, the Max Planck Society, and the Higher Education Funding Council for England. The SDSS Web Site is http://www.sdss.org/.

The SDSS is managed by the Astrophysical Research Consortium for the Participating Institutions. The Participating Institutions are the American Museum of Natural History, Astrophysical Institute Potsdam, University of Basel, University of Cambridge, Case Western Reserve University, University of Chicago, Drexel University, Fermilab, the Institute for Advanced Study, the Japan Participation Group, Johns Hopkins University, the Joint Institute for Nuclear Astrophysics, the Kavli Institute for Particle Astrophysics and Cosmology, the Korean Scientist Group, the Chinese Academy of Sciences (LAMOST), Los Alamos National Laboratory, the Max-Planck-Institute for Astronomy (MPIA), the Max-Planck-Institute for Astrophysics (MPA), New Mexico State University, Ohio State University, University of Pittsburgh, University of Portsmouth, Princeton University, the United States Naval Observatory, and the University of Washington.

This work is based in part on observations made with the *Spitzer* Space Telescope, which is operated by the Jet Propulsion Laboratory, California Institute of Technology under a contract with NASA, and on observations made with the *Chandra* X-ray Observatory, operated by the Smithsonian Astrophysical Observatory for and on behalf of NASA under contract NAS8-03060. The TKRS survey was funded by a grant to WMKO by the National Science Foundation's Small Grant for Exploratory Research program. The resulting data are a combined set of data obtained by both Team Keck and their collaborators at the University of Hawaii/Institute for Astronomy.

This study makes use of data from AEGIS, a multiwavelength sky survey conducted with the Chandra, GALEX, Hubble, Keck, CFHT, MMT, Subaru, Palomar, Spitzer, VLA, and other telescopes and supported in part by the NSF, NASA, and the STFC. Funding for the DEEP2 survey has been provided by NSF grants AST95-09298, AST-0071048, AST-0071198, AST-0507428, and AST-0507483 as well as NASA LTSA grant NNG04GC89G. The analysis pipeline used to reduce the DEIMOS data was developed at UC Berkeley with support from NSF grant AST-0071048.

Facilities: Spitzer (IRAC), Keck (DEIMOS), HST (ACS), Chandra (ACIS)

TABLE 3
Scaling Factors for Line Flux Uncertainties

Emission Line	DR7 Scale Factor	DR4 Scale Factor
[O II] λ3727	1.33	2.199
[Ne III] λ3869	1.30	1.731
Hβ	1.29	1.882
[O III]λ4363	1.15	1.306
[O III]λ4959	1.25	1.573
[O III]λ5007	1.33	1.566
[He I]λ5876	1.10	1.501
[O I]λ6300	1.02	1.378
Hα	2.06	2.473
[N II] λ6584	1.44	2.039
[S II] $\lambda\lambda$6717, 6731	1.36	1.621

TABLE 4
Scaling Factors for Uncertainties on Line Flux Ratios

Name	Emission Line Ratio	DR7 Scale Factor
Ne_3O_2	[Ne III] λ3869/[O II] $\lambda\lambda$3726, 3729	1.09
O_3	[O III] λ5007/Hβ	1.11
[O I]/Hα	[O I] λ6300/Hα	1.02
[N II]/Hα	[N II] λ6584/Hα	1.16
[S II]/Hα	[S II] $\lambda\lambda$6717, 6731/Hα	1.17
O_{32}	[O III] λ5007/[O II] $\lambda\lambda$3726, 3729	1.25
R_2	[O II] $\lambda\lambda$3726, 3729/Hβ	1.23
N_2	[N II] $\lambda\lambda$6548, 6584/Hβ	1.25
R_3	[O III] $\lambda\lambda$4959, 5007/Hβ	1.11
R_{23}	([O II] λ3727 + [O III] $\lambda\lambda$4959, 5007)/Hβ	1.20

APPENDIX

A. REVISED EMISSION LINE FLUX UNCERTAINTIES FOR SDSS DR7

The MPA/JHU analysis includes uncertainty scaling factors obtained from SDSS DR4 by comparing the spread between individual measurements for duplicate observations of the same objects with the formal errors quoted in their emission line catalogs [20]. However, this exercise was not repeated with the DR7 spectra yet there have been significant upgrades to the spectrophotometry with the latest reductions. Therefore, it is worth to revisit the line flux uncertainties.

The MPA-JHU list of duplicate spectroscopic observations was used to compute the absolute value of the difference between multiple observations of the same targets. Each pair of duplicata was considered. For a galaxy observed N times, there are $\sum_{i=1}^{N-1} i$ different pairs. For each pair, we normalize the absolute difference by the uncertainty on the difference from the catalog (i.e., the two individual uncertainties added in quadrature). If the catalog uncertainties corresponded to the true one-sigma uncertainties, 68% of the cases would be within one. Instead, the 68th percentile is always larger than one (Figure 8).

The results are tabulated for typical strong emission lines used in various galaxy evolution studies (Table 3). Relative to the previous values found for DR4 measurements, these updated uncertainty are smaller, perhaps reflecting the improved spectrophotometry in the later reductions of the spectra.

It is possible that some of this *true* albeit stasticial uncertainty may include multiplicative uncertainties that cancel out when taking the ratio of emission line fluxes. This may be especially relevant for ratios of lines that have similar wavelengths, in case of wavelength dependent uncertainties. Thus, we perform the same calculation on commonly-used line ratios as for the individual line fluxes. The results are displayed in Figure 9, and listed in Table 4. The uncertainty scaling factors are generally smaller for the line ratios than for the individual line fluxes. This trend supports the possibility that the individual line uncertainties include a multiplicative component that cancels out when taking the ratio of two lines. In other words, line ratios are better reproduced between different spectral observations of the same galaxies than the absolute flux calibration. While not surprising, it is useful to quantify this effect for studies that depend on the sample selection and for a better understanding of the latter.

B. CALCULATING AND MODELING THE OFFSETS ON THE MEX DIAGRAM

The shape of the relations describing the MEx demarcation lines are held fixed according to equations 1 and 2. We add an offset along the stellar mass axis (x) as a free parameter and, similarly to the appoach of Section 3, we adjust the best-fit to go through the region of the MEx with $0.6 < P(AGN) < 0.85$ for the upper MEx curve. Figure 10

[20] The DR4 uncertainty scaling factors and the method used to compute them are available at the following URL: http://www.mpa-garching.mpg.de/SDSS/DR4/raw_data.html

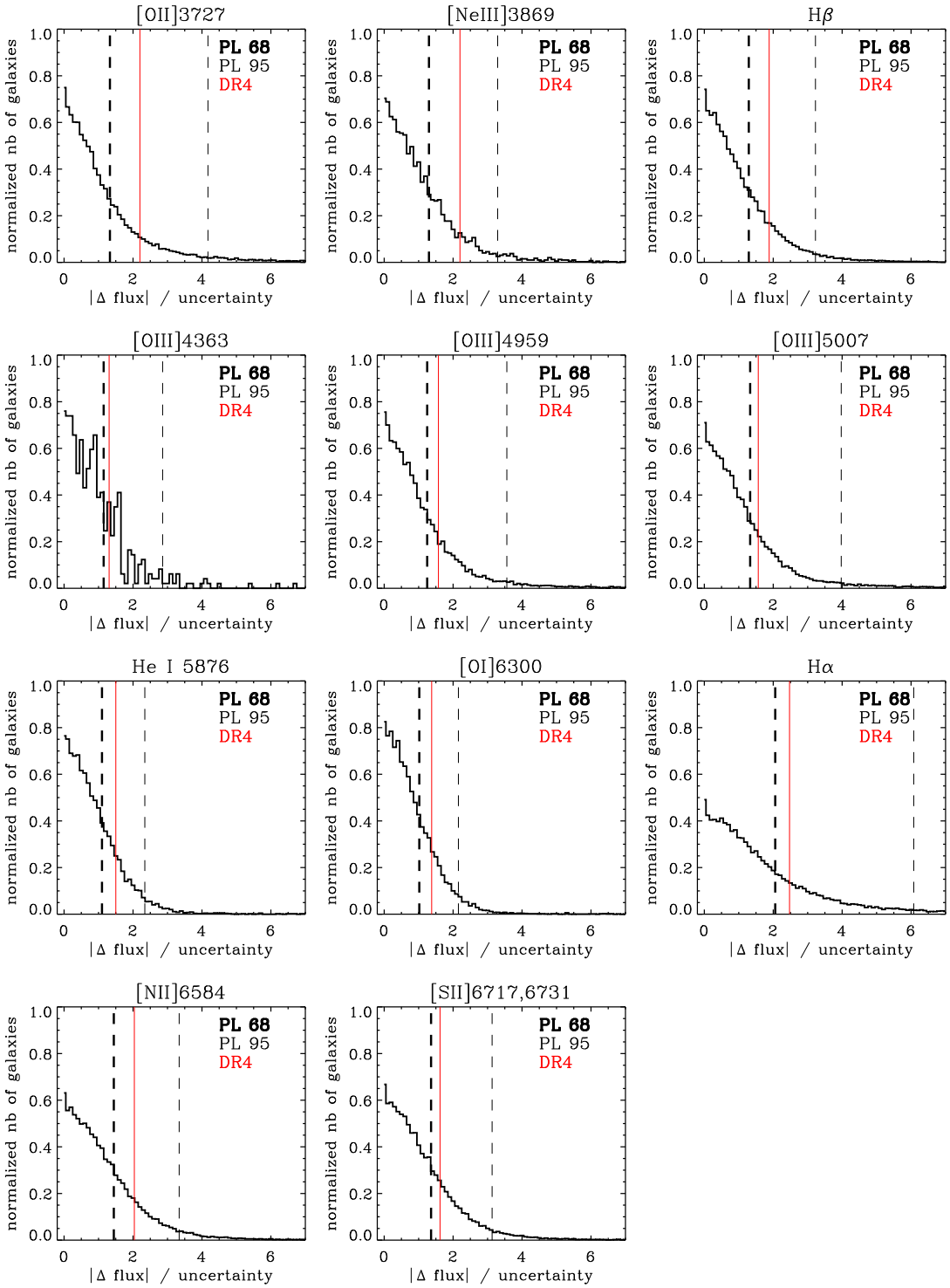

FIG. 8.— Distribution of the absolute difference between flux measurements of duplicate observations of galaxies, normalized by the catalog flux uncertainties. Each panel corresponds to a different emission line as labeled. The 68th and 95th percentiles are respectively marked with thick and thin dashed lines, while the recommended uncertainty scaling factor of DR4 is indicated with the solid red line.

illustrates the AGN probability on the MEx plane and the resulting fits for varying line luminosity thresholds.

We perform this exercise for line luminosity thresholds varying in steps of 0.1 dex and we compile the offsets in Figure 11. The automated fitting is less constrained at high luminosities ($\log(L_{line}[\mathrm{erg\,s^{-1}}]) > 40.7$) due to the small size of the prior sample when imposing a very high luminosity cut, and fails entirely above $\log(L_{line}[\mathrm{erg\,s^{-1}}]) > 41.1$. Over the range of validity, we fit the offset in $\log(M_\star)$ as a function of the threshold line luminosity with this functional form:

$$\Delta \log(M_\star) = a_0 + a_1 \times \tan^{-1}((\log(L_{line}) - a_2) \times a_3), \tag{B1}$$

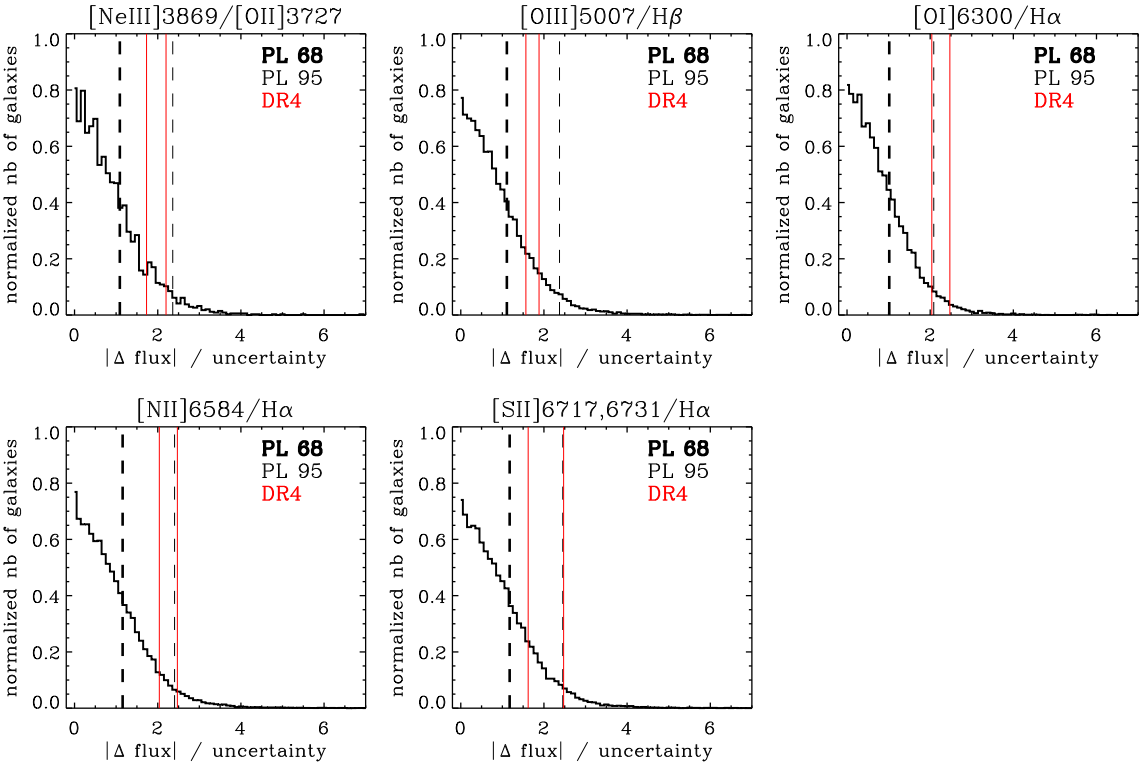

FIG. 9.— Same as Figure 8 but for emission line flux ratios, as labelled. In each panel, the recommended uncertainty scaling factors of DR4 are marked for the *individual* emission lines involved in the ratio (solid red lines; see Table 3).

where L_{line} is the threshold luminosity imposed for detection of [O III] and Hα. The coefficients are {0.28988, 0.28256, 40.479, 0.82960}.

The offsets calculated with equation B1 allows one to visualize the regions of the MEx diagram largely populated by AGN or star-forming galaxies given an effective detection limit on [O III] and Hα (e.g., Figure 10). More accurate computations of AGN (or star-forming) sample should take into account the full bivariate distribution of the prior sample. We developed routines[21] to calculate the probability of having a given excitation type (star-forming, composite, LINER, Seyfert) given the location on the MEx diagram and the flux detection limit of the survey considered. The calculations are made on a galaxy per galaxy basis, taking in each case the luminosity detection threshold at the corresponding redshift. Optionally, prescriptions for pure luminosity evolution of emission-line galaxies can be taken into account. These prescriptions are described and applied in Section 4.2 and in Appendix C.

C. SINGLE-LINE SELECTIONS

Alternatively to the scenario used in this work, one could consider a single emission line selection. We show a few such cases here, an [O III] selection where we substitute for the evolution of the knee of the [O III] luminosity function (Figure 12b), an Hα-only selection based on the detection limit and evolution of the knee of the Hα luminosity function (Figure 12a), an Hβ-selection based on the detection limit of Hβ but assuming the same evolution as the Hα luminosity function, and lastly, an Hα selection with luminosities taken at face values, without any L^* evolution correction. We also consider this null evolution scenario with a two line selection requiring both Hα and [O III] to be more luminous than the detection luminosities.

To calculate the evolution of L^* separately for Hα and [O III] emission lines, we compile values reported in the literature (Ly et al. 2007; Sobral et al. 2009; Pirzkal et al. 2013; Sobral et al. 2013; Drake et al. 2013; Colbert et al. 2013), and apply a fit of the form $L^*(z) = L^*_{z=0} \times (1+z)^n$. We solve for L^* at $z = 0$ and index n using routines from the MPFIT IDL package (Markwardt 2009).

As shown in Figure 12(a), the Hα evolution indicates a global fading of the galaxy population with time, which can be qualitatively understood as a consequence of decreasing SFRs in galaxies modulo dust attenuation, which is not included here. We find that $\log(L^*_{\rm H\alpha}) \propto (1+z)^{2.27}$ (or a log-linear fit gives $\log(L^*_{\rm H\alpha}) \propto 0.54z$, slightly steeper than the evolution of $0.45z$ reported by Sobral et al. 2013, see green points and dashed line). On the other hand, our overall best-fit evolution is slightly less steep than the reported evolution of sSFR for massive galaxies ($\propto (1+z)^{2.8}$ for 10^{10} $M_\odot$ Sargent et al. 2013, not shown), and than the $L^*_{\rm H\alpha}$ fit restricted to $z > 0.3$ (dotted line on Figure 12a), i.e., the same redshift range over which [O III] can be fitted. Some of the variation between different studies of L^* at the same redshifts could be due to cosmic variance or residual incompleteness in the sampling, but a detailed analysis

[21] Availabe at https://sites.google.com/site/agndiagnostics/home/mex

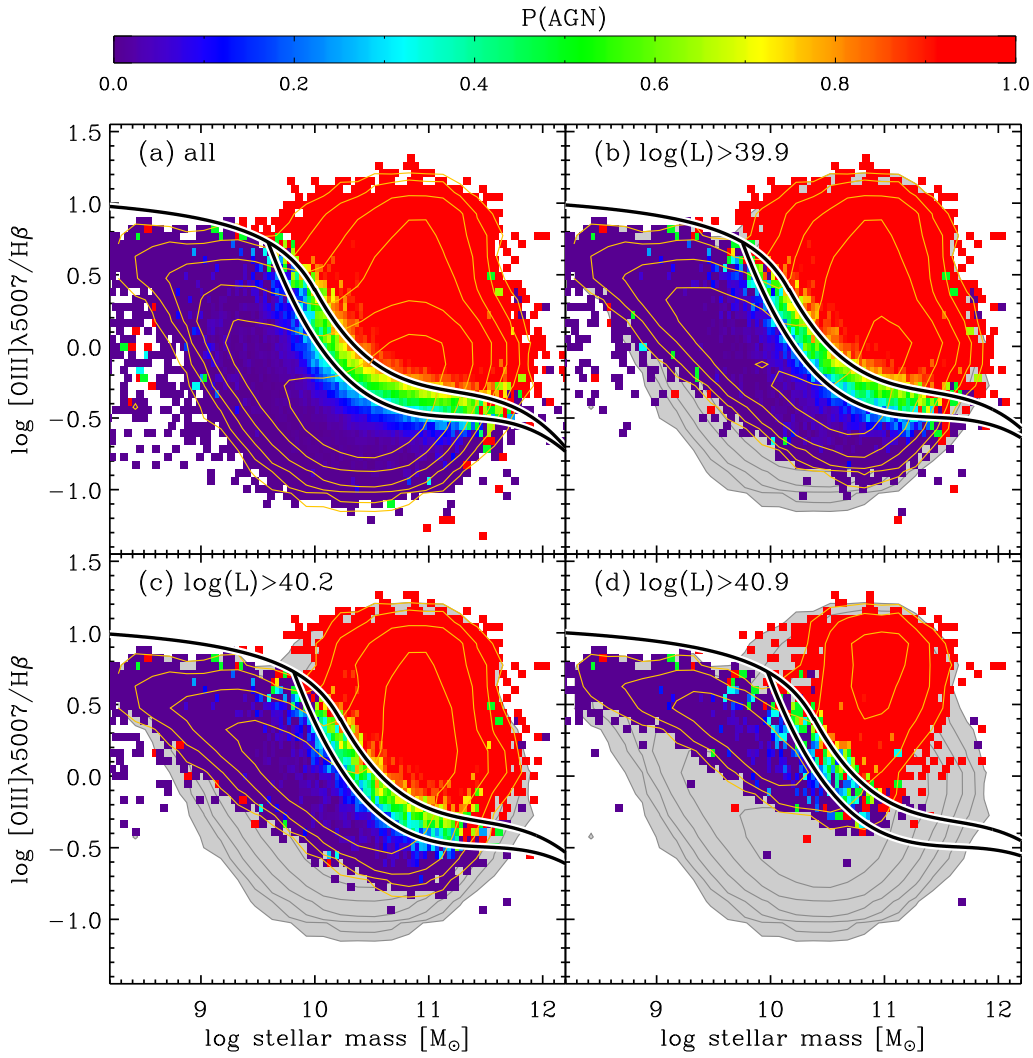

FIG. 10.— MEx diagnostic diagram. The dividing lines indicate regions corresponding to star-forming galaxies (below), MEx-intermediate galaxies (between) and MEx-AGN (above). Colored points with thin contours show the distributions of $z \sim 0$ SDSS for varying line luminosity threshold (as labeled), while the gray shaded contours include the full $z \sim 0$ prior sample. The color scheme indicates the AGN probability based on the fraction of galaxies classified as BPT-AGN in each bin (color bar). The demarcation lines are offset between each panel to encompass the transition region, where P(AGN) changes sharply from ~ 0.3 to ~ 0.8. Contours are logarithmically spaced (0.5 dex) with the outermost contour corresponding to ten galaxies per bin of 0.15 dex×0.15 dex.

is beyond the scope of this paper. Here, we adopt the best fit to all points for Hα (solid black line), which is similar to the results from Sobral et al. (2013).

For [O III] λ5007, the best-fit evolution is steeper than for Hα. We find $\log(L^*_{[\mathrm{O\ III}]}) \propto (1+z)^{4.17}$ (red curve in Figure 12), while a log-linear fit with redshift yields $\log(L^*_{[\mathrm{O\ III}]}) \propto 0.85z$. However, there is a scarcity of measurements of galaxy [O III] LFs at the lowest redshifts. Namely, we did not find such measurements at $z < 0.3$. If similar to the Hα situation, we could expect substantial scatter at a fixed redshift including at the lowest redshifts, implying that the true evolution of $L^*_{[\mathrm{O\ III}]}$ could be different from the best-fit shown here and more similar to the Hα evolution. Indeed, fitting only $z > 0.3$ points for Hα yields a steeper evolution, though still not as steep as our current best-fit case for [O III]. This reinforces the relevance to try two evolutionary scenarios for [O III] by applying the Hα evolution (panel a) and the steeper [O III] evolution (panel b), with the assumption that these two scenarios may bracket the real evolution.

Physically, we could expect that the steeper evolution seen for [O III] could be a real feature because it is qualitatively consistent with our understanding of gas-phase metallicity evolution in the sense that higher redshift galaxies had lower metallicities therefore comparatively more luminous [O III] lines. Thus, the [O III] luminosity function fading with cosmic time would then be a combination of both decreasing SFRs and increasing gas-phase metallicities in the bulk of star-forming galaxies.

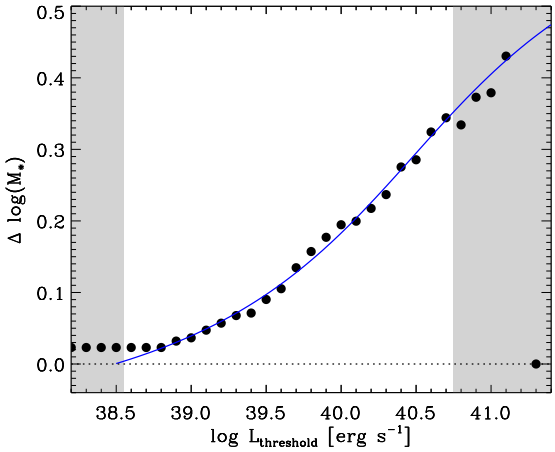

FIG. 11.— Offsets along the stellar mass axis as a function of the line luminosity threshold applied to Hα and [O III]. The offsets were calculated separately for the upper (filled circles) MEx curve and the spacing between the two curves is kept fixed. The data points were fitted with a simple analytical form over the range of validity (excluding the gray zones; equation B1).

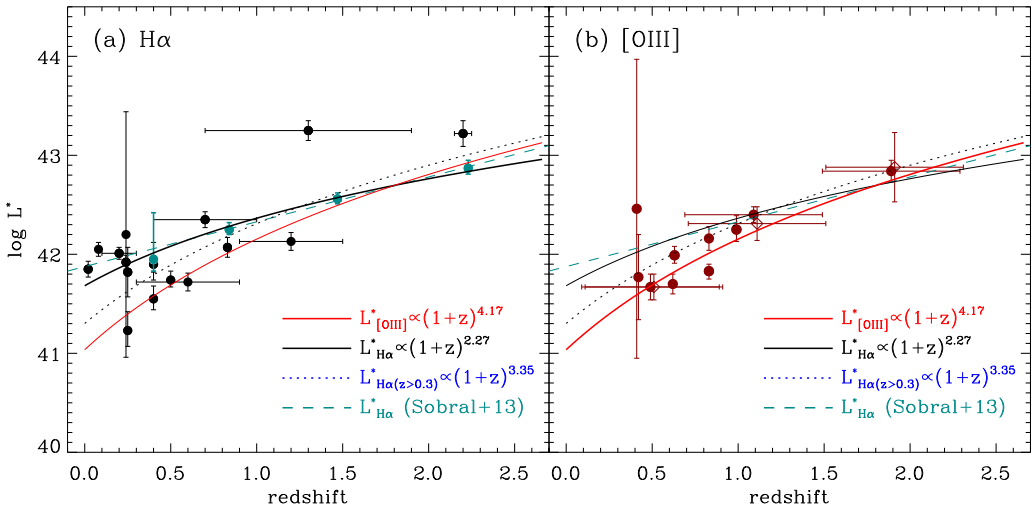

FIG. 12.— Redshift evolution of the critical value L^* of emission line luminosity functions of (a) Hα, and (b) [O III]. Values are compiled from the literature, and include a direct comparison with the evolution found by Sobral et al. (2013) in green (green filled circles and dashed line). Our best-fit evolution goes like $(1+z)^{2.27}$ for Hα (solid black curve on panel a) and like $(1+z)^{4.17}$ for [O III] (solid red curve on panel b). We also fit to Hα at $z > 0.3$ (dotted line) to enable a closer comparison with the [O III] results. In the case of [O III], two open diamond symbols show repeated measurements with fixed faint-end slope. Using these two points instead of their counterpart at $z = 1.1$ and 1.9 (slightly offset for clarity of the plotting symbols) does not noticeably change the fit.

[O III] Selection

We investigate a pure [O III] selection by applying luminosity thresholds to [O III] corresponding to the detection limit to which we subtract the evolution of $L^*_{[\mathrm{O\ III}]}$ shown in Figure 12(b) between the redshift of the sample considered and the prior reference sample at $z \sim 0.09$.

In Figure 13, we repeat the comparison with the same high-redshift samples as in Figure 5. The figures are identical except for the predicted contours, which now correspond to pure [O III] selection and $L^*_{[\mathrm{O\ III}]}$ evolution. The main differences are that (i) the AGN branch is broader and extends both to the left-most reach of the prior sample, which was previously removed by the Hα luminosity cut, and further to the right toward the locus of LINERs, which was previously removed with a more luminous [O III] cut, and (ii) the star-forming branch reaches to lower values of [O III]/Hβ, which was previously not the case due to requiring [O III] to be as luminous as Hα and applying the higher threshold corresponding to milder $L^*_{\mathrm{H}\alpha}$ evolution relative to $L^*_{[\mathrm{O\ III}]}$ evolution. This extension of the star-forming branch to lower [O III]/Hβ values worsens the agreement especially at the massive, high [N II]/Hα end of the diagrams. Similarly, the extension of the AGN contours toward the LINERs (higher stellar masses on the MEx, and higher [N II]/Hα on the BPT on the AGN side) worsens the agreement on the BPT for the T13 and N14 samples, and is unconstrained for the Y12 sample as the authors had previously removed independently identified AGNs from their parent sample and are left with fewer AGN candidates, several of them having only lower limits on [O III]/Hβ ratios. However, the agreement on the AGN side of the MEx is slightly improved for the N14 sample, which tends to be biased

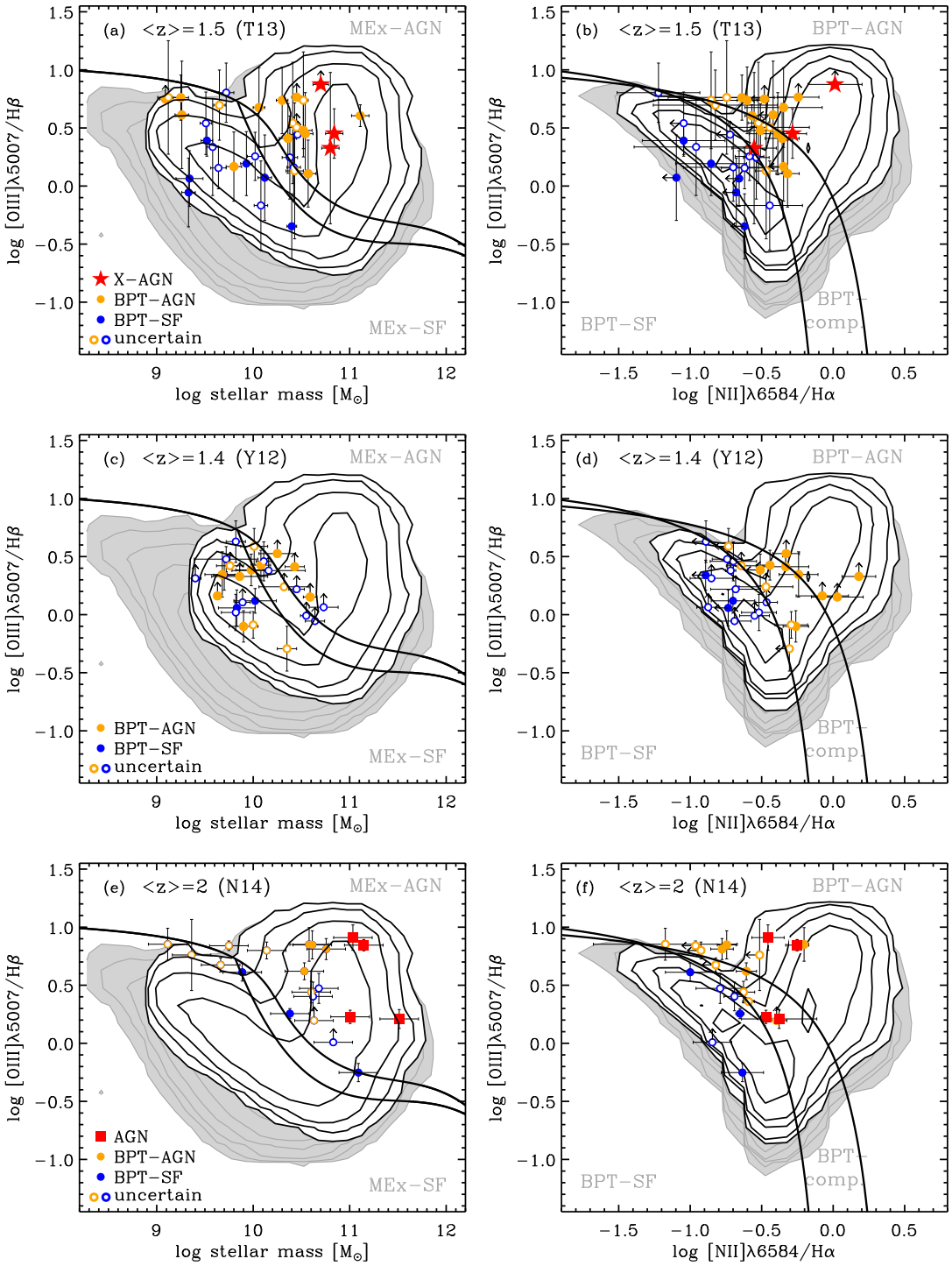

FIG. 13.— Same as Figure 5 with predicted contours corresponding to a pure [O III] selection, after accounting for $L^*_{[\mathrm{O\ III}]}$ evolution.

toward massive hosts compared to the $z \sim 1.5$ samples.

By fading the [O III] luminosities more strongly than in our fiducial approach, we draw a comparison sample that may include more metal-rich galaxies in the prior sample relative to the target higher-redshift sample. To compare with the main method adopted in this work, we revisit the predicted MZ relations in Figure 14(a,b). Relative to MZ relations predicted with the fiducial approach (Figure 7), the new predicted contours for $z \sim 0.8$ and $z \sim 1.4$ samples indeed include galaxies that are slightly more metal-rich, and more noticeably at higher masses ($> 10^{10}$ $M_\odot$) in the $z \sim 1.4$ Y12 sample. Qualitatively, the predicted trends go in the same direction as the observations, and are in fair agreement with the observations. Compared with our fiducial scenario from Figure 7, the agreement may be slightly better for the $z \sim 0.8$ sample, and slightly worse for the $z \sim 1.4$ sample, but not strikingly different.

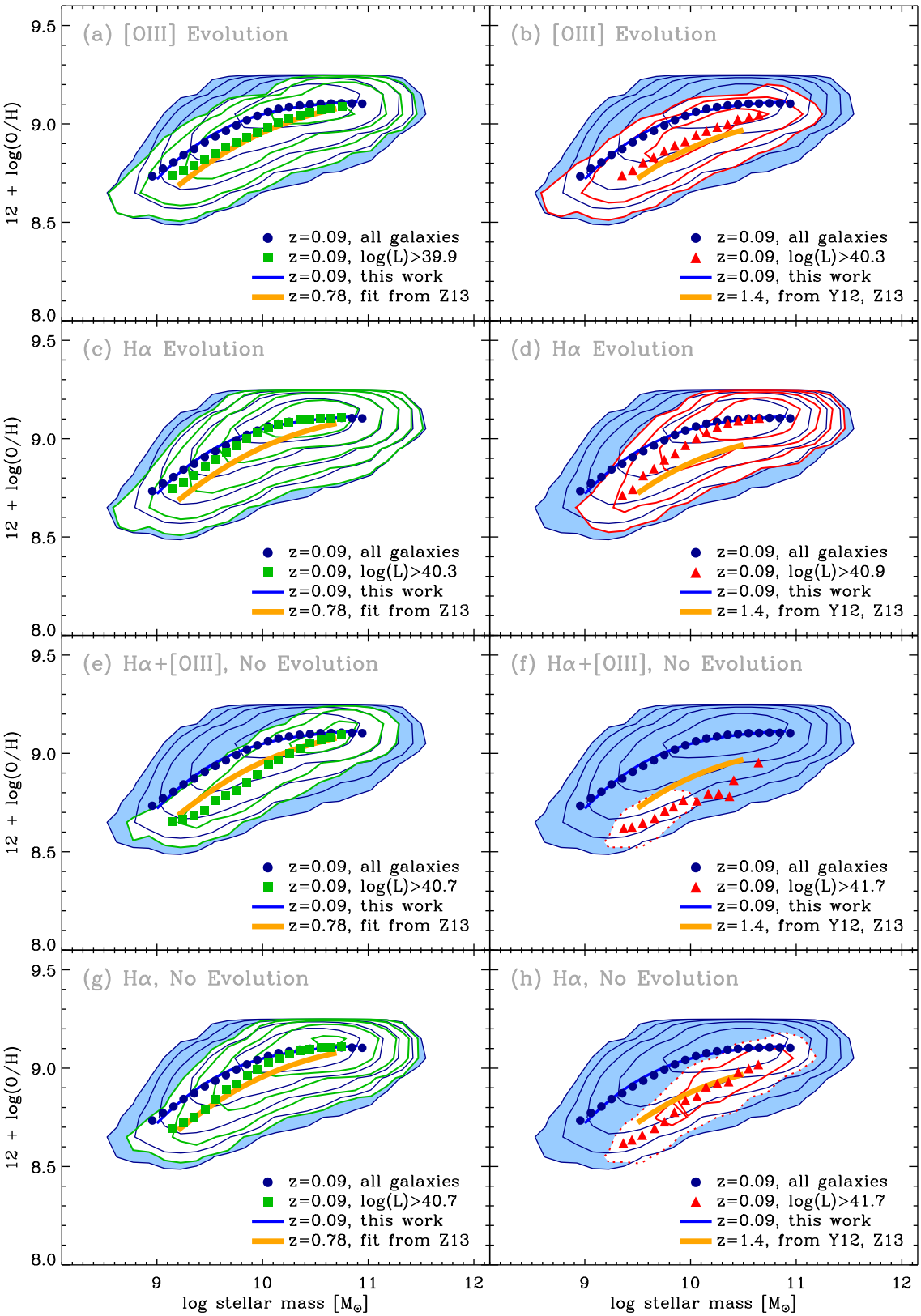

FIG. 14.— MZ relation. Each row contains a pair of panels corresponding to the labeled scenario. The left-hand panel includes a comparison to observed $z \sim 0.8$ relation from Z13, and the right-hand panel includes a comparison to observed $z \sim 1.4$ relation from the Y12 sample fitted by Z13 (orange line). The meaning of plotting symbols and contours is identical to Figure 7, except that the threshold line luminosities to make the $z \sim 0.8$ (green) and $z \sim 1.4$ (red) SDSS predictions are adjusted individually according to selection and evolution scenarios, as follows: (a,b) [O III] selection and evolution of $L^*_{[\mathrm{O\ III}]}$; (c,d) Hα selection and evolution of $L^*_{\mathrm{H}\alpha}$; (e,f) Hα+[O III] selection and no evolution; (g,h) Hα selection no evolution. Contours are logarithmically spaced (0.5 dex) with the outermost contour corresponding to 50 galaxies per bin of 0.15 dex×0.15 dex. In panels (f) and (h), we show one additional outer contour at 0.5 dex lower number density (dotted red contour) to aid the visualization of those less populated subsamples.

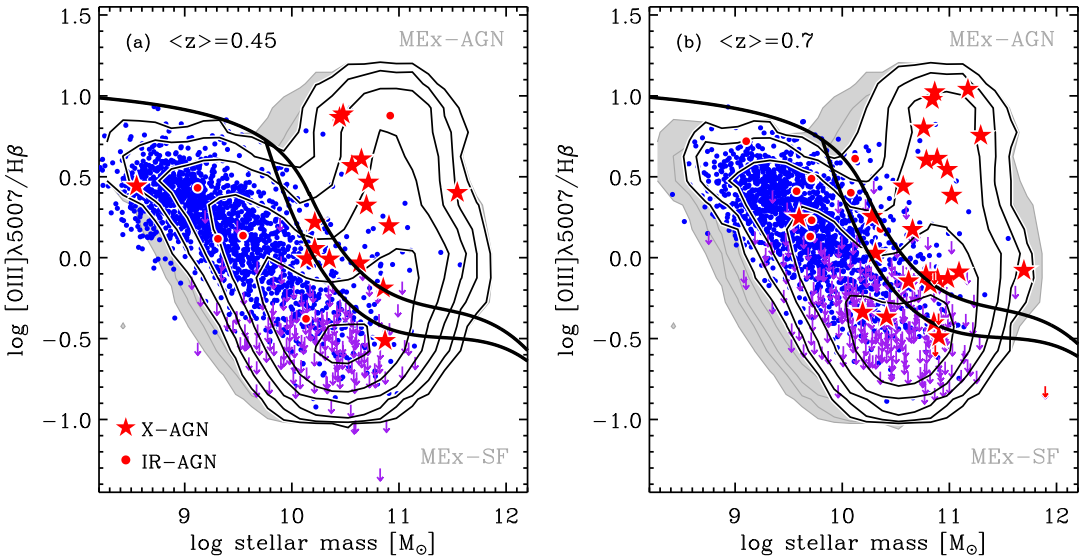

FIG. 15.— MEx AGN diagnostic diagram applied to intermediate redshift galaxies: (a) $\langle z \rangle = 0.45$, (b) $\langle z \rangle = 0.7$. Same as Figure 4 except for an Hβ selected sample. The purple downward arrows indicate [O III] upper limits and Hβ detections, and black contours show the corresponding Hβ selected prior sample. Contours are logarithmically spaced (0.5 dex) with the outermost contour corresponding to ten galaxies per bin of 0.15 dex×0.15 dex.

Hβ Selection

At intermediate redshifts where we only have Hβ and [O III], and no coverage of Hα, we perform a pure Hβ selection by keeping only galaxies with Hβ detections (3σ) and including cases where [O III] is an upper limit. We use the same $z \sim 0.45$ and $z \sim 0.7$ samples from J11 as in Section 2.2 except that we now remove Hβ upper limits, and add instead points with Hβ detections and [O III] upper limits (purple arrows on Figure 15). The predicted contours include prior galaxies with Hβ luminosities above the line flux detection threshold faded by the same evolution as Hα, and reproduce fairly well the locus of the observed points, though the constraint is weaker at low [O III]/Hβ ratios because most observations have only an [O III] upper limit in these cases.

Relative to the full prior sample (filled gray contours), this Hβ selection cuts the left-hand side of both the star-forming and AGN branches. While an [O III] selection formally cuts the bottom part of the branches. The results are fairly similar on the star-forming side because of the tilt of the branch from top left to bottom right. In details, the selections differ most strongly at the high-mass end of the star-forming branch, which is more trimmed with an [O III] selection, and at the low-mass end of the AGN branch, which is more trimmed for a Hβ selection.

Hα Selection

We repeat the analysis with a pure Hα selection for the high-redshift samples at $z > 1$. The new predicted contours are shown in Figure 16. The observed samples are the same as in Figure 5 except that we now include galaxies which have an upper limit on [O III] and therefore on their [O III]/Hβ ratios (only present in the Y12 sample). The Hα selection contours appear to overpredict the number of galaxies that should be observed at low [O III]/Hβ ratios. We recall that the T13 sample was selected from HST/grism data covering Hβ and [O III], and is effectively [O III]-selected. While in principle Hβ could be brighter than [O III], this would require very elevated SFRs given the bright flux limit (5×10^{-17} erg s^{-1} cm^{-2}) and that Hβ is intrinsically much fainter than Hα (Hβ/Hα < 0.35) while at the same time [O III]/Hα is often higher at high emission line luminosities (Ly et al. 2007; Colbert et al. 2013).

The Y12 parent selection includes as a criterion predicted Hα fluxes, but the subsample shown here is not purely Hα-selected because some galaxies with Hα detection could have upper limits to both [O III] and Hβ, preventing us from constraining their position on the BPT and MEx diagrams. Keeping this caveat in mind, Y12 still appear to be the sample best fitted by Hα selected contours on the BPT diagram relative to the T13 and N14 samples. The N14 sample is poorly represented by the contours on the star-forming side of both the MEx and BPT diagrams, with a clear overprediction of the number of galaxies with low [O III]/Hβ ratios. The contours on the MEx-AGN region encompass up to 73% (11/15) of galaxies including uncertainties, while the BPT contours appear to be a poorer representation of the data on the AGN branch by overpredicting cases with comparatively elevated [N II]/Hα.

Like the [O III] line, Hα is also sensitive to SFRs but less to metallicities. Thus, we expect that predicted MZ relations based on Hα could reach higher metallicities than an [O III] selection with the same luminosity threshold. This is indeed what we find in Figure 14(c,d). Galaxies with the highest Hα luminosities still tend to have lower metallicities at the low-mass end, but this is no longer the case at the high-mass end, where they have comparable metallicities to the full prior sample. This is particularly visible in panel (d), where the predicted red contours and triangles correspond to Hα luminosity above $10^{40.9}$ erg s^{-1}without constraints to other emission lines.

Overall, a pure Hα selection does not seem appropriate for some of the samples shown in Figures 16 and 14. However,

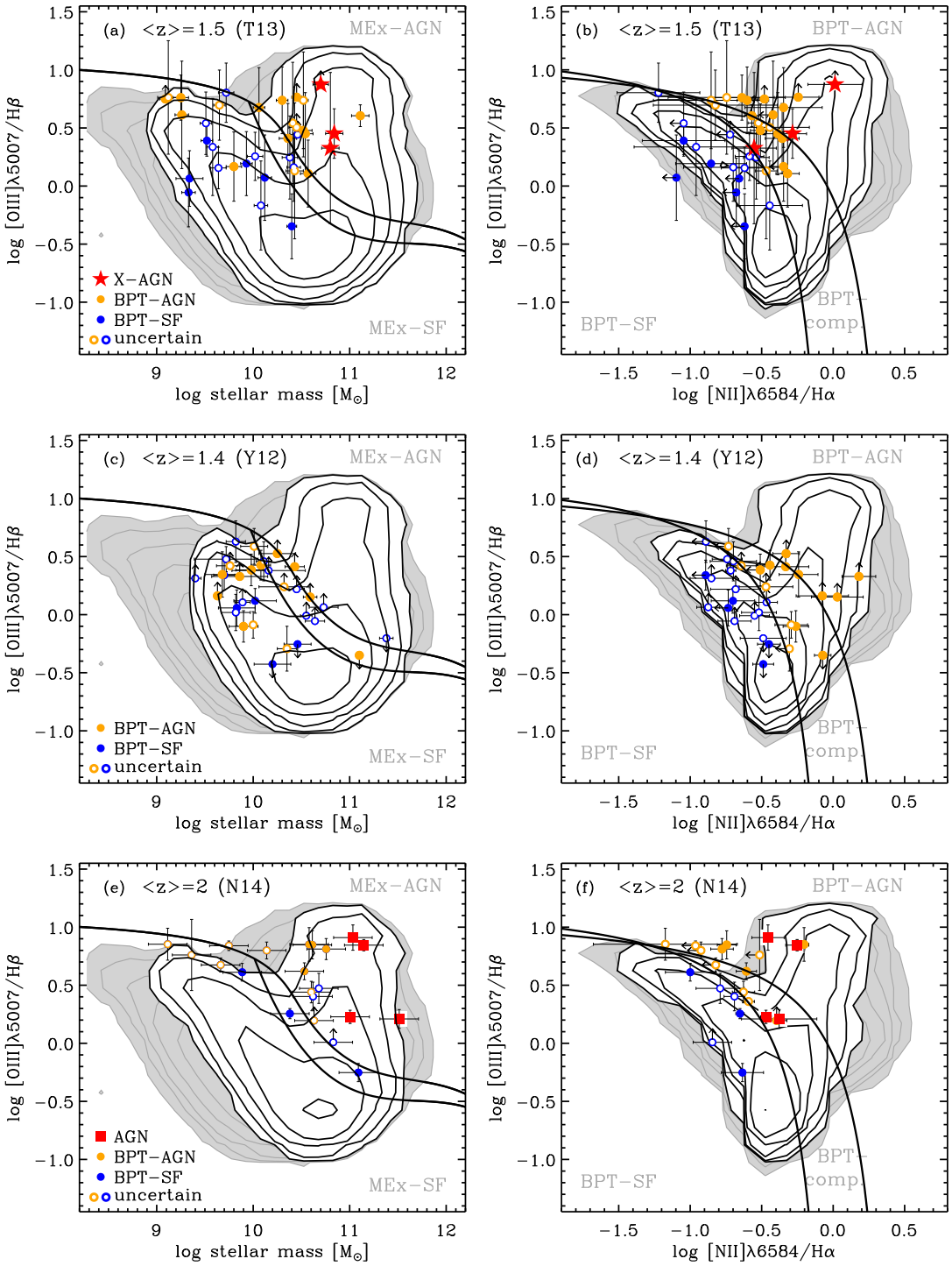

FIG. 16.— Same as Figure 5 with predicted contours corresponding to a pure Hα selection, and including $L^*_{\rm H\alpha}$ evolution.

this exercise demonstrates that a an Hα selection should in principle yield more metal-rich galaxies at high masses and therefore a weaker apparent MZ evolution at the highest mass relative to a sample for which it is required to detect other emission lines such as [O III]. Also, comparing the two scenarios from Figure 14, we can predict that Hα selected samples may thus find a steeper MZ relation than an [O III]-selected sample, or a sample requiring both [O III] and Hα. This is at least qualitatively consistent with recent work by (Zahid et al. 2013b). These authors find a steepening of the MZ relation for their $z \sim 1.6$ sample of Hα-selected galaxies (parent sample described by Kashino et al. 2013).

Null Evolution Scenario

Lastly, we consider the case where the luminosity detection threshold is taken at face value, i.e., without applying any corrections for the fading of emission line L^*. In one case, we require both Hα and [O III] to be more luminous

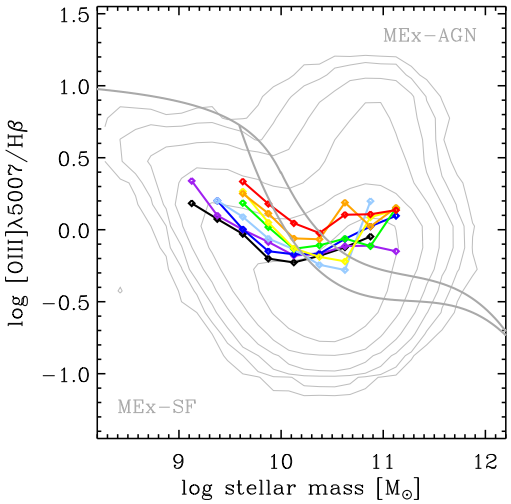

FIG. 17.— MEx diagnostic diagram of the eight redshift slices used by Vitale et al. (2013). The redshift slices are centered at z =0.21 (black), 0.27 (purple), 0.34 (blue), 0.40 (light blue), 0.59 (green), 0.67 (yellow), 0.76 (orange) and 0.84 (red). In each slice, spectra were stacked in bins of stellar mass, and the [O III]/Hβ emission line ratio was measured on the stacked spectra. A zoomed in version of these tracks was presented in Figure 6 of the article by Vitale et al. (2013). Contours show the number density of our reference $z \sim 0$ SDSS sample, and are logarithmically spaced by 0.5 dex, with the outermost contour corresponding to 10 galaxies per bin (0.15 dex×0.15 dex).

than the detection limit at the median redshift of the sample (Figure 14e,f). In the other case, the requirement is only set on Hα (Figure 14g,h). The resulting MZ predictions are made for the same $z \sim 0.8$ and $z \sim 1.4$ samples considered with alternative scenarios. When requiring both Hα and [O III] to be above the luminosity detection threshold, the MZ relation evolution is clearly overpredicted in both redshift slices, with the contours lying at lower metallicities than the observed relations. This implies that comparing high-redshift galaxies to lower redshift galaxies of the same Hα and [O III] luminosities may be too extreme as this scenario overshoots the observed evolution. On the other hand, predictions from the null evolution scenario applied only to Hα lie closer to the observed MZ relations at $z \sim 0.8$ and $z \sim 1.4$. The slope of the predicted relation is slightly steeper than observed, but not inconsistent given typical uncertainties that characterize metallicity measurements, and the spread around the mean.

For the two MZ relation samples considered here, at $z \sim 0.8$ and $z \sim 1.4$, the empirical predictions that correspond the most closely to the observations are the fiducial scenario with both Hα and [O III] lines above the threshold faded by $L^*_{\rm H\alpha}$ evolution, the [O III] only selection faded by $L^*_{\rm [O\ III]}$ evolution, and the Hα-only selection with no evolution. The data in hand do not allow us to rule out any of these three options. However, the least prefered scenarios are a pure Hα selection with $L^*_{\rm H\alpha}$ evolution, a null evolution scenario with both Hα and [O III] above the detection threshold, and using the full SDSS prior sample (blue contours and blue circles). If we may not have singled out the best scenario in absolute terms, we have demonstrated that a few sensible options are preferable than comparing high-redshift samples to the full SDSS low-redshift sample with no account of selection effects arising from emission line detection limits.

D. APPLICATION TO STACKED SPECTRA

In this Appendix, we apply our empirical prediction method to observational results published by Vitale et al. (2013). These authors stacked zCOSMOS-bright spectra in bins of redshift and stellar masses and found that the redshift tracks were systematically displaced from one other on the MEx diagram, in the sense that the higher redshift bins tend to be located above and/or to the right of the lower redshift cases (Figure 17).

Here, we attempt to reproduce these trends using a fixed flux detection limit of 10^{-17} erg s^{-1} cm^{-2} (M. Mignoli, 2013, private communication). In most redshift bins, the SDSS prior samples corresponding to the detection limit of the central redshift appear to provide us with a good representation of the star-forming branch (Figure 18) with an overall satisfactory qualitative agreement. In details, the AGN side does not show a single behavior from one redshift bin to another, and the stacked spectra tend to have fairly flat [O III]/Hβ ratios at the highest masses, while the SDSS prior distributions predict a rising AGN branch. The cause for this difference is not known but it could be related to the stacked observations containing many more non-detections than detections and/or to greater uncertainties in the line ratios of stacked spectra at the highest masses. The uncertainties are not included in the work by Vitale et al. (2013) but the numbers of objects in the highest mass bins are somewhat smaller than in the intermediate mass bins (their Table 1).

REFERENCES

Abazajian, K. N., Adelman-McCarthy, J. K., Agüeros, M. A., et al. 2009, ApJS, 182, 543
Aird, J., Coil, A. L., Moustakas, J., et al. 2012, ApJ, 746, 90
Baldwin, J. A., Phillips, M. M., & Terlevich, R. 1981, PASP, 93, 5
Barger, A. J., Cowie, L. L., Mushotzky, R. F., et al. 2005, AJ, 129, 578
Barmby, P., Alonso-Herrero, A., Donley, J. L., et al. 2006, ApJ, 642, 126
Barth, A. J., Greene, J. E., & Ho, L. C. 2008, AJ, 136, 1179

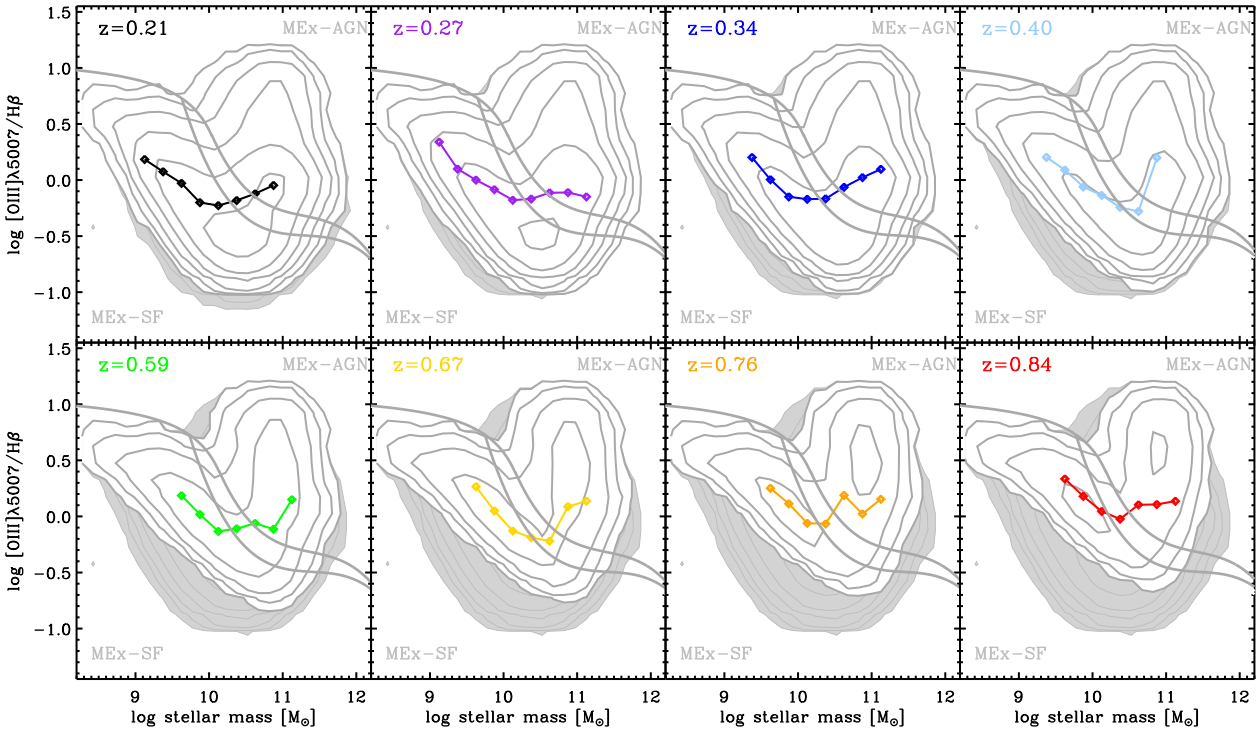

FIG. 18.— MEx diagnostic diagrams showing stacked spectra results from Vitale et al. (2013) in bins of stellar mass and redshift (colored points). Each panel contains one of the eight narrow redshift slices, labeled with the median redshift in the top left. On a given panel, the individual points correspond to stacked values in bins of stellar mass, the underlying filled gray contours encompass the full SDSS emission-line sample, while the gray contours illustrate the prediction from the prior sample tailored to the central redshift of each bin, and incorporating selection effect by applying the minimum line luminosity to [O III] and Hα in the prior sample. The tailored prior samples trace especially well the observed star-forming branch.

Bellovary, J., Volonteri, M., Governato, F., et al. 2011, ApJ, 742, 13
Bournaud, F., Dekel, A., Teyssier, R., et al. 2011, ApJ, 741, L33
Bournaud, F., Elmegreen, B. G., & Elmegreen, D. M. 2007, ApJ, 670, 237
Bournaud, F., Perret, V., Renaud, F., et al. 2014, ApJ, 780, 57
Brinchmann, J., Charlot, S., White, S. D. M., et al. 2004, MNRAS, 351, 1151
Brinchmann, J., Pettini, M., & Charlot, S. 2008, MNRAS, 385, 769
Bruzual, G. & Charlot, S. 2003, MNRAS, 344, 1000
Bundy, K., Ellis, R. S., Conselice, C. J., et al. 2006, ApJ, 651, 120
Calzetti, D., Armus, L., Bohlin, R. C., et al. 2000, ApJ, 533, 682
Cameron, E. 2011, PASA, 28, 128
Capak, P., Cowie, L. L., Hu, E. M., et al. 2004, AJ, 127, 180
Chabrier, G. 2003, PASP, 115, 763
Cid Fernandes, R., Stasińska, G., Mateus, A., & Vale Asari, N. 2011, MNRAS, 413, 1687
Cid Fernandes, R., Stasińska, G., Schlickmann, M. S., et al. 2010, MNRAS, 403, 1036
Coil, A. L., Newman, J. A., Kaiser, N., et al. 2004, ApJ, 617, 765
Colbert, J. W., Teplitz, H., Atek, H., et al. 2013, ApJ, 779, 34
Cooper, M. C., Newman, J. A., Davis, M., Finkbeiner, D. P., & Gerke, B. F. 2012, spec2d: DEEP2 DEIMOS Spectral Pipeline, astrophysics Source Code Library
Cresci, G., Mannucci, F., Sommariva, V., et al. 2012, MNRAS, 421, 262
Daddi, E., Bournaud, F., Walter, F., et al. 2010, ApJ, 713, 686
Daddi, E., Dickinson, M., Morrison, G., et al. 2007, ApJ, 670, 156
Davis, M., Faber, S. M., Newman, J., et al. 2003, in Presented at the Society of Photo-Optical Instrumentation Engineers (SPIE) Conference, Vol. 4834, Society of Photo-Optical Instrumentation Engineers (SPIE) Conference Series, ed. P. Guhathakurta, 161–172
Davis, M., Guhathakurta, P., Konidaris, N. P., et al. 2007, ApJ, 660, L1
Dekel, A. & Krumholz, M. R. 2013, MNRAS, 432, 455
Dekel, A., Sari, R., & Ceverino, D. 2009, ApJ, 703, 785
Del Moro, A., Alexander, D. M., Mullaney, J. R., et al. 2013, A&A, 549, A59
Díaz Tello, J., Donzelli, C., Padilla, N., et al. 2013, ApJ, 771, 7
Donley, J. L., Koekemoer, A. M., Brusa, M., et al. 2012, ApJ, 748, 142
Donley, J. L., Rieke, G. H., Pérez-González, P. G., Rigby, J. R., & Alonso-Herrero, A. 2007, ApJ, 660, 167
Dopita, M. A., Sutherland, R. S., Nicholls, D. C., Kewley, L. J., & Vogt, F. P. A. 2013, ApJS, 208, 10
Drake, A. B., Simpson, C., Collins, C. A., et al. 2013, MNRAS, 433, 796
Elbaz, D., Daddi, E., Le Borgne, D., et al. 2007, A&A, 468, 33
Elbaz, D., Dickinson, M., Hwang, H. S., et al. 2011, A&A, 533, A119
Elmegreen, D. M., Elmegreen, B. G., Marcus, M. T., et al. 2009, ApJ, 701, 306
Elmegreen, D. M., Elmegreen, B. G., Ravindranath, S., & Coe, D. A. 2007, ApJ, 658, 763
Erb, D. K., Shapley, A. E., Pettini, M., et al. 2006, ApJ, 644, 813
Faber, S. M., Phillips, A. C., Kibrick, R. I., et al. 2003, in Presented at the Society of Photo-Optical Instrumentation Engineers (SPIE) Conference, Vol. 4841, Society of Photo-Optical Instrumentation Engineers (SPIE) Conference Series, ed. M. Iye & A. F. M. Moorwood, 1657–1669
Ferrarese, L. & Merritt, D. 2000, ApJ, 539, L9
Förster Schreiber, N. M., Genzel, R., Bouché, N., et al. 2009, ApJ, 706, 1364
Furusawa, H., Kosugi, G., Akiyama, M., et al. 2008, ApJS, 176, 1
Gebhardt, K., Bender, R., Bower, G., et al. 2000, ApJ, 539, L13
Genzel, R., Newman, S., Jones, T., et al. 2011, ApJ, 733, 101
Giavalisco, M., Ferguson, H. C., Koekemoer, A. M., et al. 2004, ApJ, 600, L93
Greene, J. E. & Ho, L. C. 2007, ApJ, 670, 92
Grogin, N. A., Kocevski, D. D., Faber, S. M., et al. 2011, ApJS, 197, 35

Groves, B., Brinchmann, J., & Walcher, C. J. 2012, MNRAS, 419, 1402
Groves, B. A., Dopita, M. A., & Sutherland, R. S. 2004, ApJS, 153, 75
Groves, B. A., Heckman, T. M., & Kauffmann, G. 2006, MNRAS, 371, 1559
Gwyn, S. D. J. 2008, PASP, 120, 212
—. 2011, ArXiv e-prints
Hainline, K. N., Shapley, A. E., Kornei, K. A., et al. 2009, ApJ, 701, 52
Henry, A., Scarlata, C., Domínguez, A., et al. 2013, ApJ, 776, L27
Hirschmann, M., Dolag, K., Saro, A., Borgani, S., & Burkert, A. 2013, ArXiv e-prints
Holden, B. P., Oesch, P. A., Gonzalez, V. G., et al. 2014, ArXiv e-prints
Jones, T., Ellis, R. S., Richard, J., & Jullo, E. 2013, ApJ, 765, 48
Juneau, S., Dickinson, M., Alexander, D. M., & Salim, S. 2011, ApJ, 736, 104
Juneau, S., Dickinson, M., Bournaud, F., et al. 2013, ApJ, 764, 176
Kashino, D., Silverman, J. D., Rodighiero, G., et al. 2013, ApJ, 777, L8
Kauffmann et al., G. 2003, MNRAS, 346, 1055
Kelly, B. C. & Shen, Y. 2013, ApJ, 764, 45
Kennicutt, Jr., R. C. 1998, ARA&A, 36, 189
Kewley, L. J., Dopita, M. A., Leitherer, C., et al. 2013a, ApJ, 774, 100
Kewley, L. J., Dopita, M. A., Sutherland, R. S., Heisler, C. A., & Trevena, J. 2001, ApJ, 556, 121
Kewley, L. J., Groves, B., Kauffmann, G., & Heckman, T. 2006, MNRAS, 372, 961
Kewley, L. J., Maier, C., Yabe, K., et al. 2013b, ApJ, 774, L10
Kewley, L. J., Rupke, D., Zahid, H. J., Geller, M. J., & Barton, E. J. 2010, ApJ, 721, L48
Kobulnicky, H. A. & Kewley, L. J. 2004, ApJ, 617, 240
Koekemoer, A. M., Faber, S. M., Ferguson, H. C., et al. 2011, ApJS, 197, 36
Krumholz, M. & Burkert, A. 2010, ApJ, 724, 895
Lara-López, M. A., Cepa, J., Bongiovanni, A., et al. 2010, A&A, 521, L53
Lawrence, A., Warren, S. J., Almaini, O., et al. 2007, MNRAS, 379, 1599
Lehnert, M. D., Le Tiran, L., Nesvadba, N. P. H., et al. 2013, A&A, 555, A72
Lehnert, M. D., Nesvadba, N. P. H., Le Tiran, L., et al. 2009, ApJ, 699, 1660
Liu, X., Shapley, A. E., Coil, A. L., Brinchmann, J., & Ma, C. 2008, ApJ, 678, 758
Ly, C., Malkan, M. A., Kashikawa, N., et al. 2007, ApJ, 657, 738
Ly, C., Malkan, M. A., Nagao, T., et al. 2014, ApJ, 780, 122
Magdis, G. E., Daddi, E., Béthermin, M., et al. 2012, ApJ, 760, 6
Magorrian, J., Tremaine, S., Richstone, D., et al. 1998, AJ, 115, 2285
Mancini, C., Förster Schreiber, N. M., Renzini, A., et al. 2011, ApJ, 743, 86
Mannucci, F., Cresci, G., Maiolino, R., Marconi, A., & Gnerucci, A. 2010, MNRAS, 408, 2115
Markwardt, C. B. 2009, in Astronomical Society of the Pacific Conference Series, Vol. 411, Astronomical Data Analysis Software and Systems XVIII, ed. D. A. Bohlender, D. Durand, & P. Dowler, 251
Mignoli, M., Vignali, C., Gilli, R., et al. 2013, A&A, 556, A29
Moustakas, J., Zaritsky, D., Brown, M., et al. 2011, ArXiv e-prints
Mullaney, J. R., Pannella, M., Daddi, E., et al. 2012, MNRAS, 419, 95
Newman, J. A., Cooper, M. C., Davis, M., et al. 2013, ApJS, 208, 5
Newman, S. F., Buschkamp, P., Genzel, R., et al. 2014, ApJ, 781, 21
Noeske, K. G., Weiner, B. J., Faber, S. M., et al. 2007, ApJ, 660, L43
Osterbrock, D. E. & Ferland, G. J. 2006, Astrophysics of gaseous nebulae and active galactic nuclei
Pirzkal, N., Rothberg, B., Ly, C., et al. 2013, ApJ, 772, 48
Queyrel, J., Contini, T., Kissler-Patig, M., et al. 2012, A&A, 539, A93
Reddy, N., Dickinson, M., Elbaz, D., et al. 2012, ApJ, 744, 154
Reines, A. E., Greene, J. E., & Geha, M. 2013, ApJ, 775, 116
Rich, J. A., Kewley, L. J., & Dopita, M. A. 2011, ApJ, 734, 87
Rigby, J. R., Wuyts, E., Gladders, M. D., Sharon, K., & Becker, G. D. 2011, ApJ, 732, 59
Rupke, D. S. N., Kewley, L. J., & Chien, L.-H. 2010, ApJ, 723, 1255
Salim, S., Dickinson, M., Michael Rich, R., et al. 2009, ApJ, 700, 161
Salim, S., Rich, R. M., Charlot, S., et al. 2007, ApJS, 173, 267
Sargent, M. T., Daddi, E., Béthermin, M., et al. 2013, ArXiv e-prints
Savaglio, S., Glazebrook, K., Le Borgne, D., et al. 2005, ApJ, 635, 260
Shapley, A. E., Coil, A. L., Ma, C.-P., & Bundy, K. 2005, ApJ, 635, 1006
Shirazi, M., Brinchmann, J., & Rahmati, A. 2013, ArXiv e-prints
Sobral, D., Best, P. N., Geach, J. E., et al. 2009, MNRAS, 398, 75
Sobral, D., Smail, I., Best, P. N., et al. 2013, MNRAS, 428, 1128
Stasińska, G., Cid Fernandes, R., Mateus, A., Sodré, L., & Asari, N. V. 2006, MNRAS, 371, 972
Stern, D., Eisenhardt, P., Gorjian, V., et al. 2005, ApJ, 631, 163
Tacconi, L. J., Genzel, R., Neri, R., et al. 2010, Nature, 463, 781
Tanaka, M. 2012, PASJ, 64, 37
Tremonti, C. A., Heckman, T. M., Kauffmann, G., et al. 2004, ApJ, 613, 898
Trouille, L., Barger, A. J., & Tremonti, C. 2011, ApJ, 742, 46
Trump, J. R., Konidaris, N. P., Barro, G., et al. 2013, ApJ, 763, L6
Trump, J. R., Weiner, B. J., Scarlata, C., et al. 2011, ApJ, 743, 144
Ueda, Y., Watson, M. G., Stewart, I. M., et al. 2008, ApJS, 179, 124
Veilleux, S. & Osterbrock, D. E. 1987, ApJS, 63, 295
Vitale, M., Mignoli, M., Cimatti, A., et al. 2013, A&A, 556, A11
Wirth, G. D., Willmer, C. N. A., Amico, P., et al. 2004, AJ, 127, 3121
Wright, S. A., Larkin, J. E., Graham, J. R., & Ma, C. 2010, ApJ, 711, 1291
Yabe, K., Ohta, K., Iwamuro, F., et al. 2012, PASJ, 64, 60
Yates, R. M., Kauffmann, G., & Guo, Q. 2012, MNRAS, 422, 215
Yuan, T., Kewley, L. J., & Sanders, D. B. 2010, ApJ, 709, 884
Zahid, H. J., Geller, M. J., Kewley, L. J., et al. 2013a, ApJ, 771, L19
Zahid, H. J., Kashino, D., Silverman, J. D., et al. 2013b, ArXiv e-prints
Zahid, H. J., Kewley, L. J., & Bresolin, F. 2011, ApJ, 730, 137